

Fabrication and transport measurements of parallel arrays of nanowires

Master Thesis of
MARCO PFIRRMANN

Karlsruhe Institut of Technology
Department of Physics
Physikalisches Institut

Reviewer: Prof. Dr. Alexey V. Ustinov
Second reviewer: Prof. Dr. Alexander Shnirman
Advisors: Dr. Hannes Rotzinger
Dipl. Phys. Sebastian T. Skacel

19th of December 2014

Ich versichere hiermit wahrheitsgemäß, die Masterarbeit selbstständig angefertigt und die benutzten Hilfsmittel, Quellen sowie die befragten Personen und Institutionen vollständig angegeben habe. Darüber hinaus versichere ich, dass ich die Regeln zur Sicherung guter wissenschaftlicher Praxis im Karlsruher Institut für Technologie (KIT) in der gültigen Fassung beachtet habe.

Karlsruhe, 19. Dezember 2014

.....
(Marco Pfirrmann)

Contents

1	Introduction	1
2	Theoretical Background	3
2.1	Superconductivity	3
2.1.1	Ginzburg-Landau theory	4
2.1.2	Microscopic theory	5
2.1.3	Josephson Junction	5
2.2	Quasi-one-dimensional superconductor	6
2.2.1	Phase Slip	7
2.3	Phase slip centers	8
2.3.1	LAHM model of thermally activated phase slip	10
2.3.2	Quantum phase slip	11
2.4	Duality: QPS and Josephson junction	13
2.5	QPS wire arrays	16
3	Experimental Details	23
3.1	Basic idea	23
3.2	Design for a lumped QPS array	23
3.3	Design for flux localization in the array	25
4	Experimental Constraints for QPS	27
4.1	Materials in QPS studies	27
4.2	Material of choice: granular aluminium	27
4.2.1	Sheet resistance vs Argon pressure	28
4.2.2	Temperature dependence of the granular structure	29
4.2.3	Microwave properties	30
5	Sample Preparation	33
5.1	Basic fabrication concept	33
5.2	Sputter deposition	33
5.3	Thermal evaporation	33
5.4	Lithography	34
5.5	Reactive ion etching	35
5.6	Fabrication results	35
5.6.1	Electron-beam parameters	35
5.6.2	Connecting e-beam with optical lithography	37
6	Experimental Setup	39
6.1	The Cryostat	39
6.2	Measurement setup	40
6.3	Sample Holder	41

7 Experimental Results	43
7.1 Parallel array with 1 μm -nanowires	43
7.1.1 Current bias	43
7.1.2 Voltage bias	48
7.2 Parallel array with 0.75 μm -nanowires	51
7.2.1 Current bias	51
8 Conclusion	55
References	57
Appendix	61

1 Introduction

New technology gives the possibility to provide answers to long asked questions, while on the other side raise further questions for us to answer. Developments in microstructuring technology enables now controlled fabrication of quasi-one-dimensional structures, embedded in functional quantum electric circuits. In such low dimensional systems, fluctuation effects are an important subject of study, since they become more and more relevant at smaller structural sizes.

Studies on fluctuation effects in micro and nanometer size wires began in the late 1960s with the work of Little [1], analyzing the impact of phase fluctuations of the superconducting order parameter, the phase slip. Thermally activated phase slip effects (TAPS) were observed and theoretically described [2, 3] at temperatures little below T_c , as a resistive tail in measurements. While these vanish at temperatures well below T_c , observations in the late 1980s proposed phase slip effects [4] due to quantum tunneling, quantum phase slip (QPS). Extensive measurements on quantum phase slip effects in superconducting nanowires began in the mid 1990s. In 2006 Mooij and Nazarov [5], predicted a theoretical duality of the QPS physics to the well studied Josephson junction which is used for a long time in quantum circuits. Microwave measurements performed by the group of Astafiev et al. [6], showed coherent quantum phase slip effects, using single nanowires. The combination of the right material together with modern fabrication technology enabled a systematic study of phase slip effects at low temperatures. An array of parallel nanowires is the next step in this process, opening doors to new scientific discoveries expected from the duality to Josephson junction arrays.

Arrays of nanowires made out of granular aluminium are the subject of this thesis. With an in house deposition process, design and sample preparation process were optimized and transport measurements on arrays on parallel nanowires at milli-Kelvin temperatures were performed.

In chapter two, the theoretical background required for this thesis are introduced, followed by the design considerations for lumped element arrays and arrays with flux localization. Chapter four focuses on experimental constraints, comparing the material used in this thesis to the former experiments mentioned above. The sample preparation process in chapter five is followed by the experimental setup for measurements in ultra low temperatures. In chapter seven, experimental results of transport measurements on parallel nanowire arrays are presented, indicating a classical phase slip effect.

2 Theoretical Background

2.1 Superconductivity

Superconductivity, discovered as the missing electrical resistance in metals below a certain critical temperature T_c , was first seen by Kamerlingh Onnes in 1911, when he studied the temperature dependence of the resistivity in different metals [7]. This was only possible due to the cryogenic developments at that time, making such low temperatures experiments for the first time possible. The importance therein can be seen in the fact that the Nobel prize awarded to Kamerlingh Onnes two years later was not for the discovery of superconductivity, but for him developing a key technology: the method to liquefy helium.

In 1933 Walther Meissner and Robert Ochsenfeld discovered that superconductors expel an applied magnetic field from its inside, the Meissner effect [8]. The exterior magnetic field is shielded by setting up circulating currents near its surface to cancel the field within the material.

The first description of superconductivity was developed by brothers Heinz and Fritz London in 1935 [9]. They were able to describe the Meissner effect, but gave no additional hints about the physical origin of superconductivity. Their phenomenological theory is based on the Drude model, neglecting the collisions inside the superconductor. This provides the first London equation, with the current density \vec{j} , the density of superconducting electrons n_s , the electrical charge e , the electron's mass m_e , and the electric field \vec{E}

$$\frac{d\vec{j}}{dt} = \frac{n_s e^2}{m_e} \vec{E} \quad (2.1)$$

By using Faraday's law of induction and integrating over time, we get the second London equation with the magnetic flux density \vec{B}

$$\text{curl } \vec{j} = -\frac{n_s e^2}{m_e} \vec{B} \quad (2.2)$$

With Ampère's circuital law and the two London equations we can explain the Meissner effect. Inside the superconductor, the magnetic field falls off exponentially, with a significant length λ_L : the London penetration depth.

$$\lambda_L = \sqrt{\frac{m_e}{\mu_0 n_s e^2}} \quad (2.3)$$

2.1.1 Ginzburg-Landau theory

In 1950, Ginzburg and Landau published a phenomenological theory to describe superconductivity [10]. The free energy F is expressed as a function of an order parameter Ψ , which expresses the degree of order across a phase transition. The great idea behind the Ginzburg-Landau theory was, to introduce a collective wave function for the superconducting electrons $\Psi(\vec{r}) = |\Psi| \exp(i\phi(\vec{r}))$ being the order parameter. The free energy can be expressed by the free energy in the normal phase F_n , the phenomenological parameters α and β , an effective mass $m^* = 2m_e$, the electron charge e , the magnetic vector potential \vec{A} , and the magnetic flux density $\vec{B} = \nabla \times \vec{A}$.

$$F(\Psi) = F_n + \alpha|\Psi|^2 + \frac{\beta}{2}|\Psi|^4 + \frac{1}{2m^*} \left| \left(-i\hbar\nabla - 2e\vec{A} \right) \Psi \right|^2 + \frac{|\vec{B}|^2}{2\mu_0} \quad (2.4)$$

The ansatz for the GL equations is to minimize the free energy with respect to the order parameter $\frac{\delta F}{\delta \Psi^*} = 0$, leading to

$$\alpha\Psi + \beta|\Psi|^2\Psi + \frac{1}{2m^*} \left(-i\hbar\nabla - 2e\vec{A} \right)^2 \Psi = 0 \quad (2.5)$$

$$\vec{j} = \frac{2e}{m^*} \left\{ \Psi^* \left(-i\hbar\nabla - 2e\vec{A} \right) \Psi + cc. \right\} \quad (2.6)$$

For $T < T_c$ there is a non-trivial minimum in the free energy at

$$|\Psi|^2 = -\frac{\alpha_0(T - T_c)}{\beta} \quad (2.7)$$

The two differential equations (2.5) and (2.6) predict two characteristic lengths:

The **coherence length** ξ describes the distance over which the order parameter can vary due to fluctuations

$$\xi = \sqrt{\frac{\hbar^2}{4m|\alpha|}} \quad (2.8)$$

The **penetration depth** λ from the London theory can be derived, a characteristic length over which the magnetic field decays.

$$\lambda = \sqrt{\frac{m}{\mu_0 e^2 4\Psi_0^2}} \quad (2.9)$$

Using equation (2.6) the **quantization of the magnetic flux** Φ can be derived. The current density vanishes if we choose a closed loop integral path inside the superconductor. For a current flowing around a loop \vec{A} crossed by a magnetic flux density \vec{B} we find the magnetic flux to be quantized to integer numbers of a flux quantum $\Phi_0 = \frac{h}{2e}$

$$\Phi = \vec{A} \cdot \vec{B} = \frac{h}{2e}n = n\Phi_0, \quad n \in \mathbb{Z} \quad (2.10)$$

In the description above the equilibrium case is assumed. The free energy does, in first order, not change with variation of the order parameter. In the time-dependent Ginzburg-Landau theory the variation of the free energy density $f = \frac{dF}{dV}$ with the order parameter is assumed to be proportional to the relaxation rate [11]

$$\frac{\partial}{\partial t} \Psi \propto \frac{1}{\tau_{GL}} \frac{\partial f}{\partial \Psi^*} \quad (2.11)$$

with the Ginzburg-Landau relaxation time $\tau_{GL} = \frac{\pi\hbar}{8k_B(T_c - T)}$.

2.1.2 Microscopic theory

The microscopic theory of superconductivity (BCS theory) was developed by Bardeen, Cooper, and Schrieffer in 1957 [12, 13] and awarded with the Nobel prize in 1972. For the matter in this thesis, a qualitative understanding of the BCS theory is sufficient and will be explained in the following.

Superconductivity is based on an attractive potential between electrons via electron-phonon interaction, forming a bound state: a Cooper pair. The bosonic electron-electron pairs form a superconducting condensate, an analog to a Bose-Einstein condensate. All Cooper pairs condense in a (energetically favored) common ground state, separated by a energy gap Δ from the non-superconducting state

$$\Delta(T=0) = 1.76 \cdot k_B T_c \quad (2.12)$$

The superconductor is described by a single macroscopic wave function Ψ with Cooper pair density n_s and collective phase ϕ

$$\Psi = \sqrt{n_s} \exp(-i\phi) \quad (2.13)$$

The coherence length in the BCS theory ξ_{BCS} depends on Δ and the Fermi velocity v_F

$$\xi_{BCS} = \xi_0 = \frac{2\hbar v_F}{\pi \Delta} \quad (2.14)$$

Zero resistance can be explained by scattering theory. All final states of a inelastic scattering process (resistance in a wire) are energetically higher than the superconducting ground state. The energy gap Δ is too big to overcome for electrons with $E_{kin} < \Delta$, non-resistivity is the lowest energy state possible.

Before we now explore the superconductivity in nanowires, we first take a little detour and take a look at the Josephson junction (JJ). The Josephson junction is a well studied device in superconducting quantum circuits, to which we will later map the physics studied in this thesis.

2.1.3 Josephson Junction

Figure 2.1 shows two weakly coupled superconducting electrodes: a Josephson junction [14].

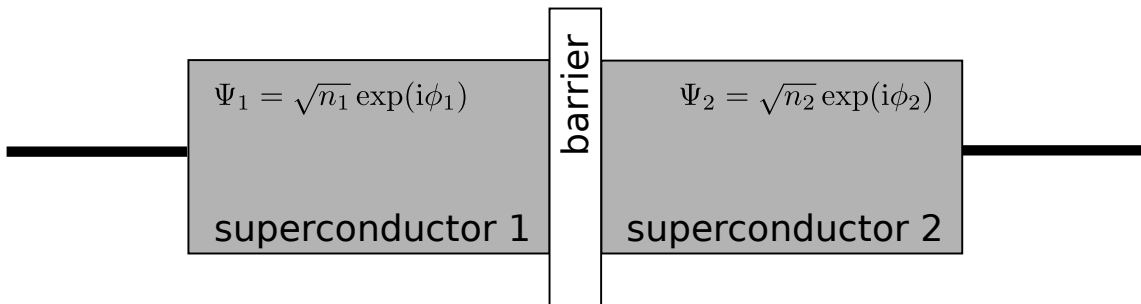


Figure 2.1: A Josephson junction consists of two superconducting electrodes connected by a weak link. The coupled system can be treated as a two-level system.

The junction can be modeled as a two-level system, with a coupling term K connecting the electrodes. They are both described by their own collective wave function Ψ_j , with n_j being the Cooper pair density and ϕ_j the collective phase in electrode j .

$$\Psi_j = |\Psi_j| \exp(i\phi_j) = \sqrt{n_j} \exp(i\phi_j) \quad (2.15)$$

For the ansatz and derivation of the Josephson equations, see for example [15]. The weak coupling results in two equations for the junction. The first equation describes the current I through the junction (Eq. (2.16)). It has a sine dependence on the phase difference $\varphi = \phi_2 - \phi_1$ across the junction with a maximum or critical current I_c . The second equation describes the voltage V behavior, being proportional to the time derivative of φ (Eq. (2.17)).

$$I = \frac{dn_1}{dt} = I_c \sin \varphi, \quad I_c = \frac{2K}{\hbar} \sqrt{n_1 n_2} \quad (2.16)$$

$$\frac{d}{dt} \varphi = \frac{2e}{\hbar} V \quad (2.17)$$

The junction shows different behavior for either DC or AC voltage bias. A DC bias voltage V_0 results in a rapid fluctuation of the sine, which causes the current to vanish. There is only a current present, if there is no voltage drop across the junction and the phase difference stays constant. By applying an additional AC voltage $V(t) = V_0 + v \cos(\omega t)$ with $v \ll V_0$ we find resonances in the voltage characteristics. This results in a DC current through the junction for AC voltages with the resonance frequency ω

$$\omega = n \cdot \frac{2e}{\hbar} V_0, \quad n \in \mathbb{Z} \quad (2.18)$$

The junction acts as a perfect frequency-to-voltage converter. Experimentally, these resonances were first seen by Shapiro in 1963 [16].

2.2 Quasi-one-dimensional superconductor

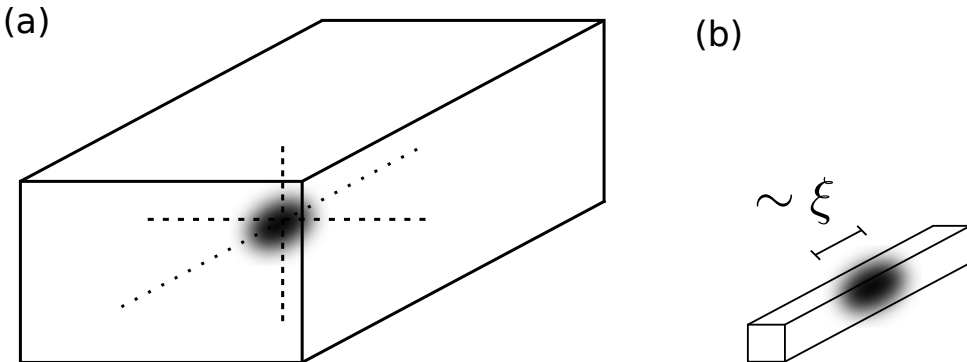


Figure 2.2: (a) In a 3D superconductor fluctuations are shunted by the superconducting material around and no voltage drop occurs. (b) If the wire dimensions are in the range of the coherence length, the fluctuation occupies in the whole wire. A voltage drop occurs across the fluctuating region.

A superconducting wire with cross sections in the order of the coherence length ξ can be regarded as a quasi-one-dimensional system. At that dimension size, fluctuations become relevant for the electric transport properties. In a bulk system, the fluctuations get shunted by the surrounding regions and can be compensated. This is not possible in the quasi-one-dimensional system.

Fluctuations in reduced systems are well known, an example being the Mermin-Wagner theorem [17]. It states that ferromagnetism does not occur in lower dimensional systems. Fluctuations in the superconducting order parameter lead to a small region of the wire going into the normal state on a timescale $\sim \frac{\hbar}{\Delta}$. The macroscopic wave function is no longer a single-valued function and the phase can change by $\pm 2\pi$. It “slips” one winding.

2.2.1 Phase Slip

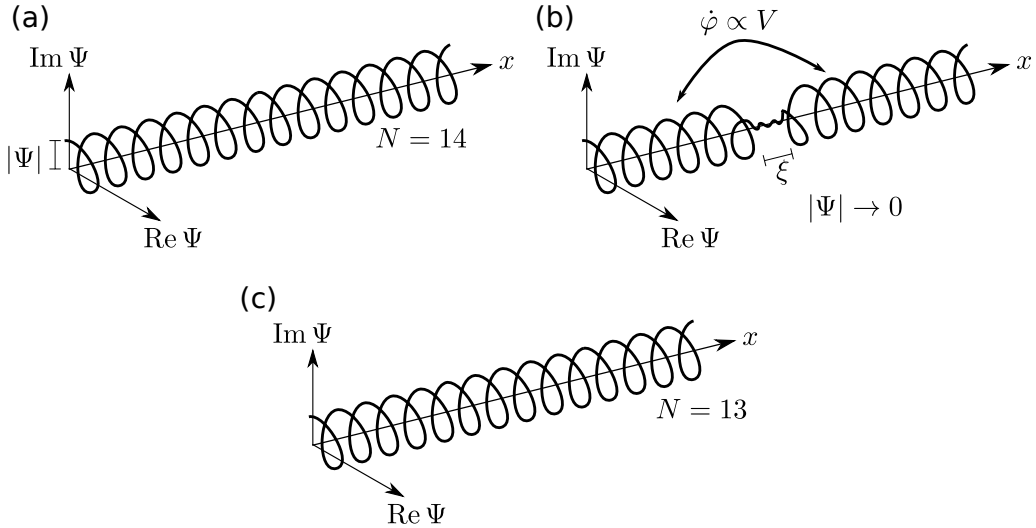


Figure 2.3: (a) Supercurrent in a thin wire with absolute value $|\Psi|$ and phase φ in the complex plane. (b) Thermal fluctuations let the order parameter vanish and the phase can change by 2π . (c) After the phase slip, superconductivity gets restored, but the winding number has changed.

Resistance in quasi-one-dimensional superconductors below the critical temperature T_c because of phase slip processes was proposed by Little [1].

The principle phase slip concept is shown in figure 2.3. A current through a thin wire with a 2π -periodicity in the phase is depicted by the helical structure along the x -axis. Due to fluctuations, the order parameter vanishes on a length of the coherence length ξ . The macroscopic wave function Ψ is no longer single-valued and the phase φ can change by $\pm 2\pi$, losing or adding one winding. The wire regains the superconducting state again, $|\Psi|$ gets restored and is again single-valued. The change of phase leads to a voltage spike across the fluctuation. This is expressed in the second Josephson equation (Eq. (2.17)), with the Josephson junction showing a similar effect

$$\frac{d\varphi}{dt} \propto V \quad (2.19)$$

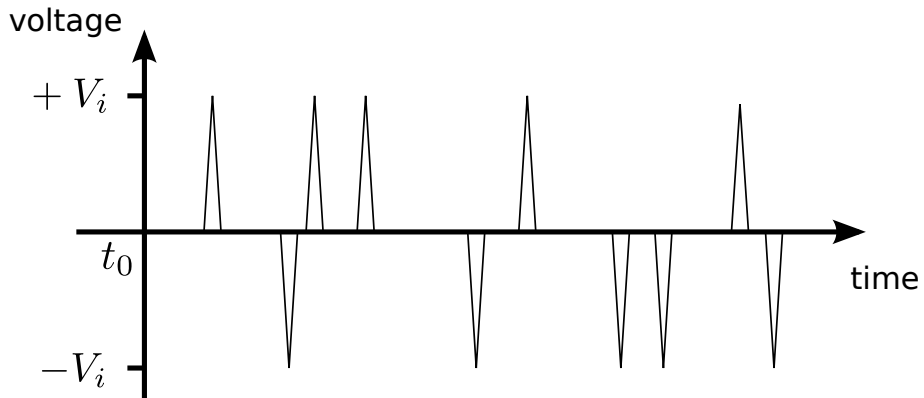


Figure 2.4: Without biasing, phase slips in both directions, creating opposite signs voltage spikes, are equally distributed.

If there is no biasing, both ± 1 phase slip events have the same probability. The median voltage $\langle V \rangle$ can be expressed by the voltage spikes V_i . For a time $T \gg \frac{\hbar}{\Delta}$, the opposite sign voltage spikes are equally distributed and cancel the net voltage

$$\langle V \rangle = \frac{1}{T} \int_{t_0}^{t_0+T} V_i dt = 0 \quad (2.20)$$

With a bias on the other hand, one phase slip direction gets more likely and a net voltage drop occurs across the wire. That means we can observe phase slips, but only in the response of the system to our biasing. Depending on how the bias occurs (DC or AC in current or voltage), the system response changes.

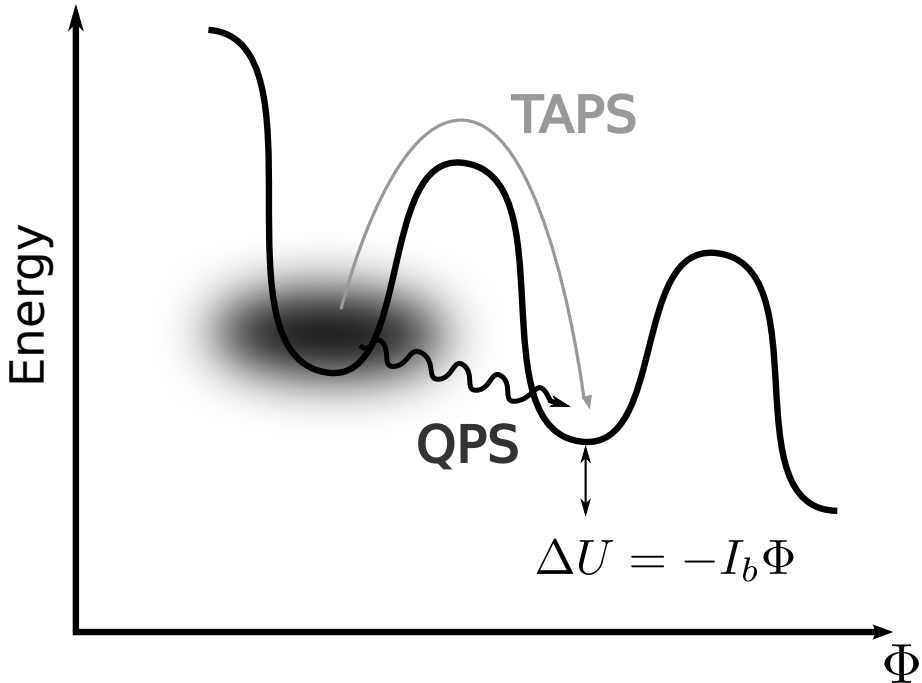


Figure 2.5: Diagram to show the different type of phase slips. The barrier can be overcome either by thermal activation (TAPS) or quantum tunneling (QPS). Based on [18].

In order to suppress the order parameter, an energy barrier needs to be overcome. Thinking of similar problems, this can be either done by thermal activation or by tunneling through the barrier and we can differ between thermally activated phase slips (TAPS) and quantum phase slips (QPS). An energy diagram showing the different phase slip types is depicted in figure 2.5. The black energy curve is similar to a tilted washboard potential (see excursion on page 12), where the superconducting quantum state sits in a minimum point.

2.3 Phase slip centers

One possibility for a phase slip process is explained by the phase slip center model developed by Skocpol, Beasley, and Tinkham [19] based on studies by Meyer and Mingerode [20, 21].

A thin superconducting film does not undergo a phase transition, when a current $I > I_C$ is applied to it. The sample is driven to the normal state, but its ability to withstand higher magnetic fields increase with decreasing thickness. Even if the current reaches I_C , the magnetic field created by this current is smaller than the critical field, the free energy

of the superconducting state remains below the normal state free energy [22]. Neglecting the magnetic field generated by the current, we get from Ginzburg-Landau (Eq. (2.4))

$$F_s = F_n - |\alpha|n_s + \frac{\beta}{2}n_s^2 + n_s \frac{m}{2}v_s^2 \quad (2.21)$$

The last term describes the kinetic energy of the superconducting electrons with velocity \vec{v}_s . We find minimum at

$$n_s = \frac{(|\alpha| - \frac{m}{2}v_s^2)}{\beta} \quad (2.22)$$

with the supercurrent density $j_s = n_s e v_s$. We see here the different dependencies from the superconducting velocity. As the superconducting current density increases, the velocity increases also. But the electron density decreases, limiting the superconducting current because the electron density is reached. There are not enough charge carriers for higher currents left.

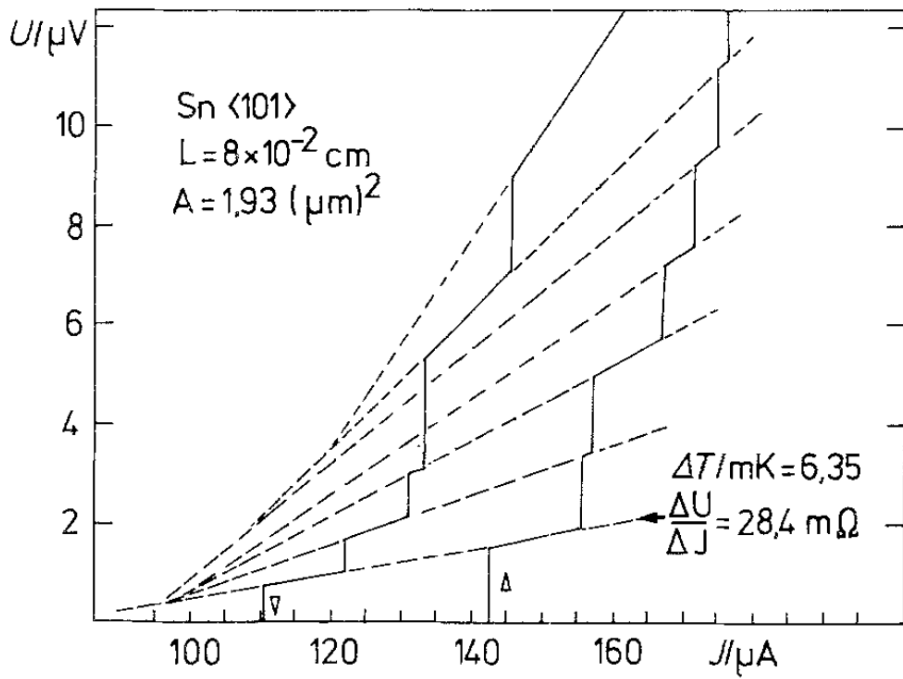


Figure 2.6: Equivalent circuit of our experimental setup featuring DC transport measurements using four-point probe with a microwave bias.

The current-voltage characteristic of a thin wires shows a stepwise increasing of the voltage. This was explained by the phase slip center model. Suppose that the thin wire has a weak spot, a structural defect at a certain location where the current reaches its critical value at first. Any further increase in the current leads to a flow of normal electrons which create an electric field. The field accelerates them to their critical velocity, Cooper pairs are broken up. The amplitude of the order parameter vanishes, But since the superconducting state remains favored, the amplitude gets restored. At any cycle, the phase of the order parameter to the left and right of the weak spot will change by 2π , naming it phase slip center.

2.3.1 LAHM model of thermally activated phase slip

The first quantitative analysis of thermally activated phase slip experiments was done by Langer and Ambegaokar in 1967 [2]. They derived a transmission rate Γ_{LAHM} for TAPS, starting at the time-dependent Ginzburg-Landau theory.

$$\Gamma_{LAHM}(T) = \Omega_{LAHM}(T) \exp\left(-\frac{\Delta F(T)}{k_B T}\right) \quad (2.23)$$

with the attempt frequency Ω_{LAHM} and the free energy ΔF from the Ginzburg-Landau theory (Sec. 2.1.1). This energy has to be overcome thermally to cause a phase slip. The attempt frequency $\Omega_{LAHM} = \frac{N_e}{\tau_e}$ depends on the number of superconducting electrons N_e and a time scale for electron-electron collision $\tau_e \sim 10^{-12}$ s.

Following this approach, McCumber and Halperin used the Ginzburg-Landau time τ_{GL} to describe the time scale of a phase slip [3]. The attempt frequency was calculated in more detail to

$$\Omega_{LAHM}(T) \propto \frac{1}{\tau_{GL}} \sqrt{\frac{\Delta F(T)}{k_B T}} \frac{L}{\xi} \quad (2.24)$$

with the length L and the coherence length ξ of the wire. The energy barrier to pass can be expressed by the critical field H_c and the cross section A of the wire

$$\Delta F(T) \propto H_c^2 A \xi \quad (2.25)$$

If the wire is biased by a DC current I_s , each phase slip releases an energy of $I_s \Phi_0$. This energy is dissipated into the environment and has to be carried away in order to maintain superconductivity. This problem is explained further in section 2.5. The energy barrier changes to

$$\Delta F^\pm = \Delta F \pm \frac{\Phi_0 I_s}{2} \quad (2.26)$$

This leads to an effective voltage drop

$$\begin{aligned} V &= \Phi_0 [\Gamma_{LAHM}^+ - \Gamma_{LAHM}^-] \\ &= 2\Phi_0 \Omega_{LAHM} \exp\left(-\frac{\Delta F(T)}{k_B T}\right) \sinh\left(\frac{\Phi_0 I_s}{2k_B T}\right) \end{aligned} \quad (2.27)$$

By an ohmic approach $R = \frac{V}{I_s}$ and approximating $\sinh x \approx x$ for small bias currents $I_s < \frac{2k_B T}{\Phi_0}$ we get the wire resistance

$$\begin{aligned} R_{LAHM} &= 2\Phi_0 \Omega_{LAHM} \exp\left(-\frac{\Delta F(T)}{k_B T}\right) \frac{\Phi_0}{2k_B T} \\ &= R_q h \frac{\Omega_{LAHM}}{k_B T} \exp\left(-\frac{\Delta F(T)}{k_B T}\right) \end{aligned} \quad (2.28)$$

with the quantum resistance $R_q = \frac{h}{4e^2} \approx 6.45 \text{ k}\Omega$. The LAHM model was confirmed in studies on the current-voltage characteristic and resistive transition of Sn whisker crystals [23, 24]. It is only valid for temperatures just below T_c , since the attempt frequency and the free energy barrier vanish approaching T_c .

2.3.2 Quantum phase slip

Going to temperatures $T \ll T_c$ the probability of TAPS is reduced. In this case, a nanowire should become superconducting again. But several studies on different materials hint at a non-zero resistance far away from the critical temperature [4, 25–29]. In Fig. 2.7 the original plot from [26] is printed, showing finite resistance in MoGe wires far from T_c . This resistance can be explained with quantum tunneling of the order parameter, leading to a phase slip: The quantum phase slip (QPS).

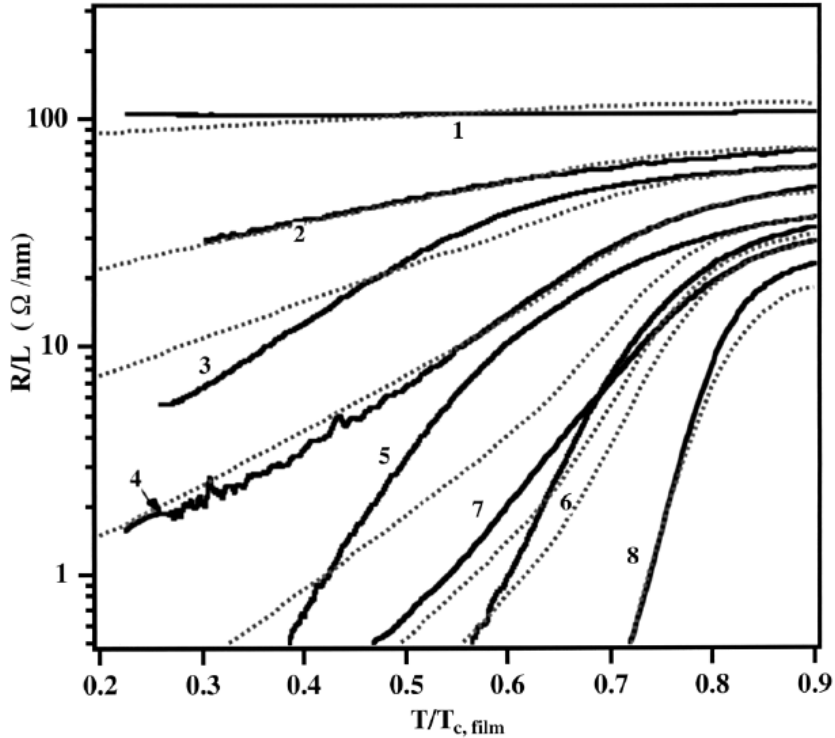


Figure 2.7: Original plot from [26]. Resistance per unit length vs normalized temperature was measured. The solid lines are the measured data, the dotted lines are calculated by taking the LAHM model and QPS effects into account (Eq. 2.34).

The attempt to describe QPS was inspired by the LAHM theory. The relevant thermal energy scale $k_B T$ was replaced by a energy scale $\frac{\hbar}{\tau_{GL}}$, based on the Ginzburg-Landau time.

$$k_B T \rightarrow \frac{\hbar}{\tau_{GL}} \Rightarrow \Gamma_{QPS} \propto \Omega_{QPS} \exp\left(\frac{\Delta F_{QPS} \cdot \tau_{GL}}{\hbar}\right) \quad (2.29)$$

The conclusion by Giordano [4, 30] was only conceptionally successful. The model could only explain the behavior for long ($l > 200$ nm) wires [31]. The estimation for the exponent was too high [32], meaning the probability would not be sufficient enough to observe QPS. A more heuristic formulation was presented in [26], following Giordano's approach of replacing the energy scale.

The exponent can be estimated using BCS theory for dirty superconductor [33]. For $T = 0$ K we find

$$\frac{\Delta F_{QPS} \cdot \tau_{GL}}{\hbar} \propto \frac{R_q}{R_N} \frac{l}{\xi} = \frac{R_q}{R_\xi} \quad (2.30)$$

with the quantum resistance R_q , wire length l , coherence length ξ and total normal state resistance of a wire R_N . R_ξ is the normal resistance of a wire in a length ξ

$$R_N \frac{\xi}{l} = R_\square \frac{l}{w} \frac{\xi}{l} = R_\square \frac{\xi}{w} = R_\xi \quad (2.31)$$

The same can be done for the QPS attempt frequency Ω_{QPS} . Using equations 2.24 and 2.30 we find

$$\Omega_{QPS} \propto \frac{l}{\xi} \sqrt{\frac{R_q}{R_\xi}} \frac{1}{\tau_{GL}} \quad (2.32)$$

With $\frac{1}{\tau_{GL}} \propto k_B T_c$ we find for the QPS tunneling rate,

$$\Gamma_{QPS} = \alpha \cdot \frac{l}{\xi} \sqrt{\frac{R_q}{R_\xi}} k_B T_c \exp\left(-\beta \frac{R_q}{R_\xi}\right) \cdot \hbar \quad (2.33)$$

using α and β as proportionality constants. This equation states, that the QPS tunneling rate depends in principle on the exponent, coherence length ξ and on the normal resistance of a wire in a length ξ . This means, that the QPS rate can be tuned by the right material (parameters ξ and R_\square) with appropriate wire dimensions ($R_\xi \propto w$). The parameter β cannot be influenced and is in order 10^{-1} . The prefactor parameters l and T_c are in comparisons of little account.

The resistance coming from QPS can be calculated similar to equations 2.27 and 2.28, leading to a total resistance R

$$R = \left[R_N^{-1} + (R_{LAHM} + R_{QPS})^{-1} \right]^{-1} \quad (2.34)$$

A microscopic QPS model was developed by Golubev and Zaikin [32, 34], coming to a similar result. Comparing the two QPS models we find a common exponential term, but an additional prefactor $\sqrt{\frac{R_q}{R_\xi}}$ in the Golubev-Zaikin approach. This resulted in a rather large fit parameter α in the data in [26].

Excuse: RCSJ model of a Josephson junction

The resistively and capacitively shunted junction model (RCSJ) is used for a classical description of the electrodynamics of a Josephson junction (JJ). A perfect JJ, shunted by a resistance R and a capacitance C models a real junction (see fig 2.8).

Describing the current through the parallel circuit and using the Josephson equations (2.16) and (2.17) we find

$$I = I_c \sin \varphi + \frac{\Phi_0}{2\pi} \frac{1}{R} \frac{d}{dt} \varphi + \frac{\Phi_0}{2\pi} C \frac{d^2}{dt^2} \varphi \quad (2.35)$$

This can be seen as an equation of motion of a particle, moving in the “tilted washboard” potential $U(\varphi)$

$$U(\varphi) = -I_c \frac{\Phi_0}{2\pi} \left(\frac{I}{I_c} \varphi + \cos \varphi \right) = -E_j \cos \varphi - \frac{\Phi_0}{2\pi} I \varphi \quad (2.36)$$

with the Josephson energy $E_j = \frac{\Phi_0}{2\pi} I_c$. The behavior of a particle in the washboard potential depends on the current through the junction. The ratio I/I_c in equation (2.36) tends to tilt the potential. This is shown in figure 2.8. Depending on this tilt, a particle is trapped in a potential minimum ($I < I_c$) or it “runs” down the washboard ($I > I_c$). Due to thermal fluctuations or quantum tunneling however, the particle can overcome the barrier and change its quantum state. This causes a finite voltage to appear [35, 36].

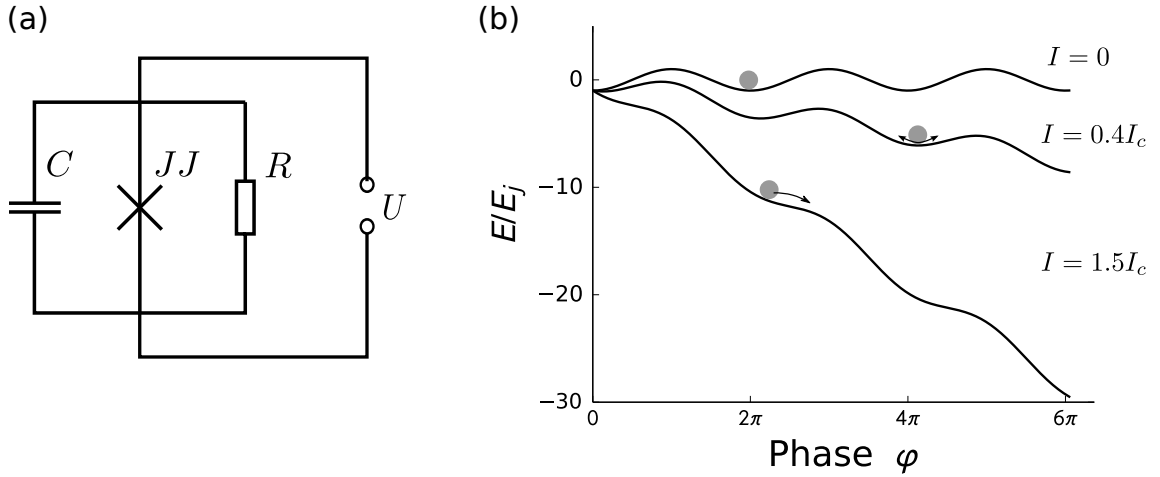


Figure 2.8: (a) A physical Josephson junction is modeled using a shunt resistance and shunt capacitance. (b) Tilted washboard potential for the different settings, $I = 0$, $0 < I < I_c$ and $I > I_c$.

2.4 Duality: QPS and Josephson junction

In 2006, Mooij and Nazarov explored a method to connect quantum phase slip with the Josephson effect [5], using a well known classical duality between magnetic flux and electrical charge. This was motivated by comparing the energy spectrum of a Cooper pair box (see for example [37]), a quantum circuit containing a Josephson junction (Fig. 2.9(d)), to the energy spectrum of a QPS nanowire in a ring structure (Fig. 2.9(a)). Coherent QPS, a coupling between distinct macroscopic quantum states preserving the phase, were assumed, characterizing the junction by the transition energy $E_s/2$ with $E_s = \hbar\Gamma_{QPS}$ (see page 16). The nanowire acts here as a QPS junction with C_{kin} and L_{kin} , where frequent QPS are expected if $Z_c > R_q$ [32].

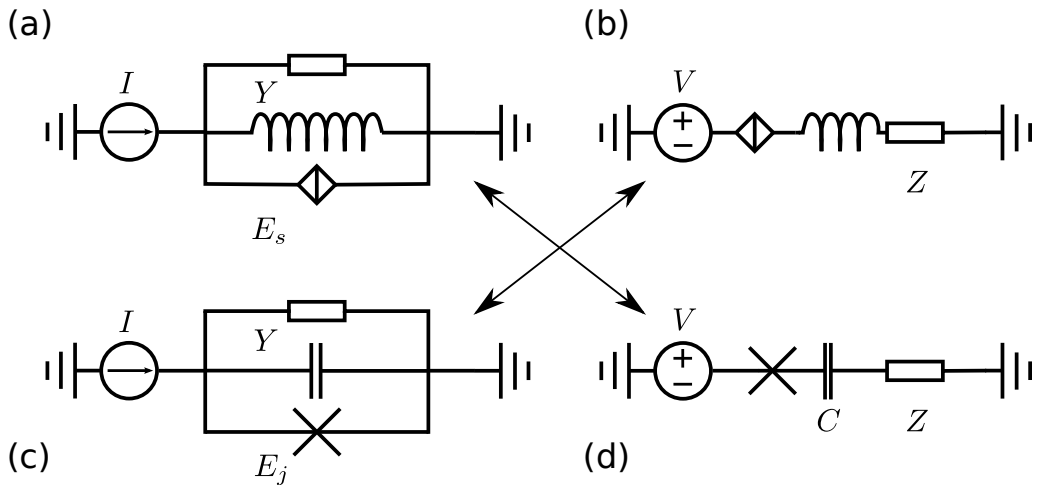


Figure 2.9: The duality of QPS and Josephson junction allows the mapping of quantum circuits, depicted by the arrows in the middle. Analog to [5].

The Cooper pair box consists of a Josephson junction with a series capacitor C . The junction is voltage biased by a voltage V over the capacitor. An island for Cooper pairs on one side of the junction to one plate of the capacitor is created. The pairs condense in one macroscopic ground state $|n\rangle$ (charge number state), with n representing the number

of additional Cooper pairs on the island. The capacitive energy E_C depends parabolically on the gate-induced charge $n_g = Q/2e = CV/2e$ in units of Cooper pairs.

$$E_C = (n - n_g)^2 \quad (2.37)$$

The energy crosses at half integer values of n_g . The system couples across the Josephson junction by the Josephson energy E_J , creating a two level system with the states $|n\rangle$ and $|n+1\rangle$ representing two adjacent number of Cooper pairs. The coupling lifts the degeneracy in E_C and the energy splits with E_J for $E_J \ll E_C$. The whole spectrum is periodic in the offset charge n_g , leading to the periodic energy spectrum in figure 2.10 (a). The splitting is formed similar to the electric band structure in solids.

Writing down the Hamiltonian we find

$$H_{JJ} = E_c (n - n_j)^2 - \left(\frac{E_J}{2} \sum_n |n+1\rangle \langle n| + \text{h.c.} \right) \quad (2.38)$$

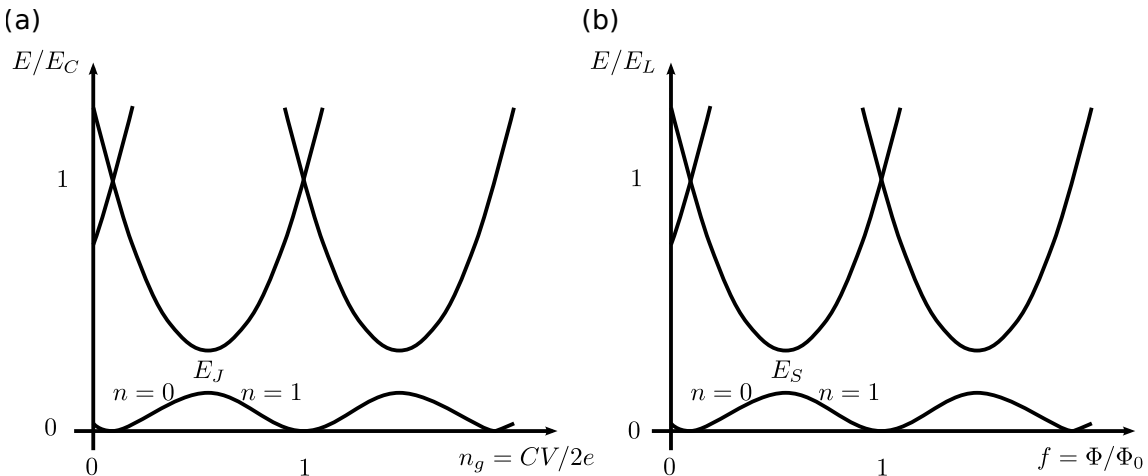


Figure 2.10: Energy diagrams for the (a) Cooper pair box (Fig. 2.9(d)) and (b) a parallel QPS junction (Fig. 2.9(a)). Both circuits represent two-level systems, forming periodic energy band. Analog to [5].

A similar behavior can be found in the QPS junction. The inductive energy $E_L = \frac{\Phi_0^2}{2L}$ depends parabolically on the applied flux $f = \Phi/\Phi_0$ in numbers of flux quanta with the integer n representing here the fluxoid number inside the loop. The phase slip energy $E_S = \hbar\Gamma_{QPS}$ creates an energy splitting if $E_S \ll E_L$ at half integers fluxoid numbers. The states $|n\rangle$ and $|n+1\rangle$ represent states with adjacent number of fluxoids.

$$H_{QPS} = E_L (n - f)^2 - \left(\frac{E_S}{2} \sum_n |n+1\rangle \langle n| + \text{h.c.} \right) \quad (2.39)$$

We find similarities in the Hamiltonians, being equivalent by exchanging

$$E_L \leftrightarrow E_C; \quad E_J \leftrightarrow E_S; \quad n_g \leftrightarrow f \quad (2.40)$$

The difference in the energy scale favors a relevant quantum number, either phase or charge. In the Cooper pair box, $E_C \gg E_J$, the charge is well defined compared to the phase, while the QPS junction is in the limit of weak phase slips ($E_L \gg E_S$) with a well

defined phase. Phase and charge are canonically conjugated variables, with the operators for charge \hat{q} and phase $\hat{\phi}$ satisfying the commutation relation

$$[\hat{q}, \hat{\phi}] = -i \quad (2.41)$$

with \hat{q} in units of $-2e$. The Hamiltonians can be written with these operators and using the junction energy coming from the tilted washboard potential (Eq. (2.36)).

$$\text{JJ} : H = E_C \hat{q}^2 - E_j \cos \hat{\phi} \quad (2.42)$$

$$\text{QPS} : H = \frac{E_L \hat{\phi}^2}{(2\pi)^2} - E_s \cos(2\pi \hat{q}) \quad (2.43)$$

By applying the canonical transformation

$$(\hat{q}, \hat{\phi}) \rightarrow \left(-\frac{\hat{\phi}}{2\pi}, 2\pi \hat{q} \right) \quad (2.44)$$

to the QPS Hamiltonian we transform it into the Josephson Hamiltonian without changing the commutation relation, e.g. (2.41). The QPS junction is the exact dual to the well studied Josephson junction with respect to the transformations taking place by substituting the parameters

$$E_s \leftrightarrow E_j, E_L \leftrightarrow E_C, I \leftrightarrow V/R_q \quad (2.45)$$

This mapping opens new possibilities. We are able to predict transport properties of QPS wires on the basis of the well studied Josephson junction. The current characteristic of a Josephson junction with a localized phase in a minimum of the tilted washboard potential (Fig. 2.8(b)) is described in equation (2.35):

$$I = I_c \sin \varphi + \frac{\Phi_0}{2\pi R} \frac{1}{dt} \frac{d}{dt} \varphi + \frac{\Phi_0}{2\pi} C \frac{d^2}{dt^2} \varphi \quad (2.46)$$

The duality mapping leads to the voltage characteristic of a QPS wire

$$V(t) = V_c \sin(2\pi q) + 2e \left(L \frac{d^2 q}{dt^2} + R \frac{dq}{dt} \right) \quad (2.47)$$

or, in the DC case with no time dependence

$$V_{DC} = V_c \sin(2\pi q) \quad (2.48)$$

with a critical voltage

$$V_c = \frac{2\pi}{(-2e)} E_s \quad (2.49)$$

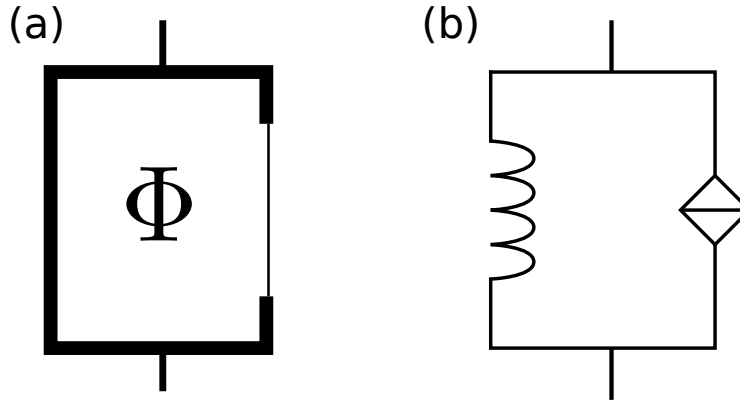


Figure 2.11: (a) Proposed loop structure containing a QPS wire to observe coherent quantum phase slip effects. (b) Schematic circuit. Analog to [38].

Coherent quantum phase slip

The duality was proposed assuming coherent quantum phase slip. So far, only incoherent quantum phase slip events were observed and studied. The incoherent phase slip is a stochastic process leading to dissipation in the system. The emission is spontaneous and corresponds to an infinite number of modes. Contrary to individual QPS, coherent QPS cannot be separated into individual events and it would be wrong to say that coherent QPS describe a quantum mechanical coherent sequence of such individual quantum phase slips. Coherent coupling preserves the phase information. This can only happen, if the coupling takes place between distinct macroscopic quantum states. Comparing it to a Josephson junction, CQPS is the counterpart of charge tunneling through the junction. Instead of a charge, a magnetic flux tunnels through the nanowire.

In order to observe CQPS, various experiments have been proposed [39, 40] and performed since proposing the duality [6, 41–44]. Most of them inspired by a parallel QPS junction design [38], a two-level system shown in figure 2.11. The two-level system is detected by a two-tone microwave spectroscopy. The coupling can be identified in the transmission measurement by a loss of energy. This energy is absorbed and drives the transition. The measurement scheme is depicted in figure 2.12. The first tone determines the flux value f in the system, while the second tone measures the transition frequency for this very spot. This is done for multiple flux values across the energy splitting. The minimum in the transition energy is directly at the splitting, with the transition frequency giving the splitting energy, in this case E_S .

Coherent QPS behavior was found by Astafiev and co-workers in 2012 [6], thus validating the duality between QPS and Josephson junction.

2.5 QPS wire arrays

During a phase slip event the energy gets dissipated in the non-dissipative superconducting system. In order to maintain superconductivity it is crucial to transport the heat away from the experiment as fast as possible. The size difference of the nanowires and the surrounding leads result in an impedance mismatch which slows down the heat transport. The problems get reduced by using not a single wire, but an array of parallel nanowires. This system is interesting for studies also because of more fundamental physics.

The Josephson junctions are used together with the definition of the second based on the caesium 133 atomic clock, as a “conventional” volt definition [45], since acts as a perfect frequency-to-voltage converter based solely on natural constants (Fig. 2.13(a)).

$$V_N = N \cdot \frac{\hbar}{2e} f \quad (2.50)$$

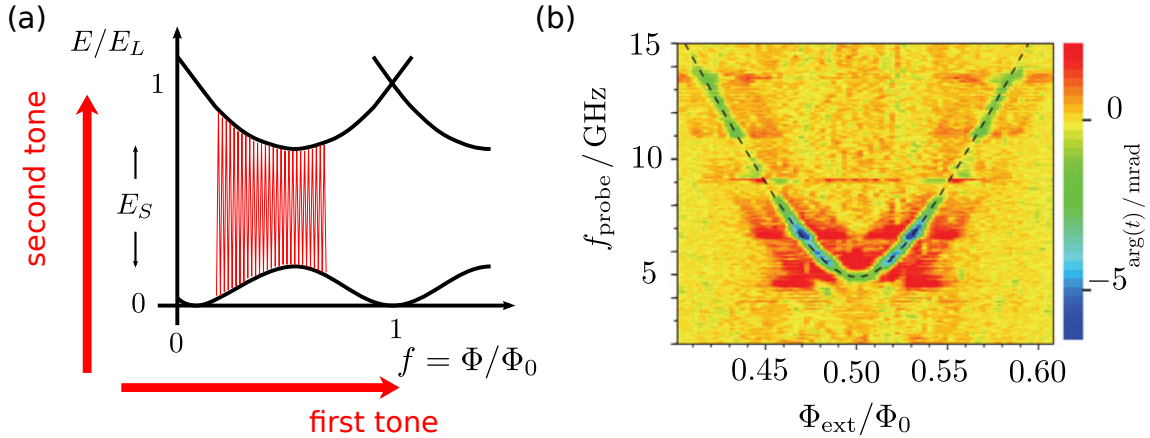


Figure 2.12: (a) Principle of two-tone spectroscopy. The energy spectrum is analog to figure 2.10(b). The first tone sets the flux value (motion in along flux-axis) and the second tone sweeps the energy for every flux value. This is pictures by the red line inside the energy spectrum. (b) Original plot from [6]. The minimum in the transition corresponds to the energy splitting. The color indicates the amount of energy transferred, getting smaller going to blue colors. This indicates the energy is absorbed and drives the transition.

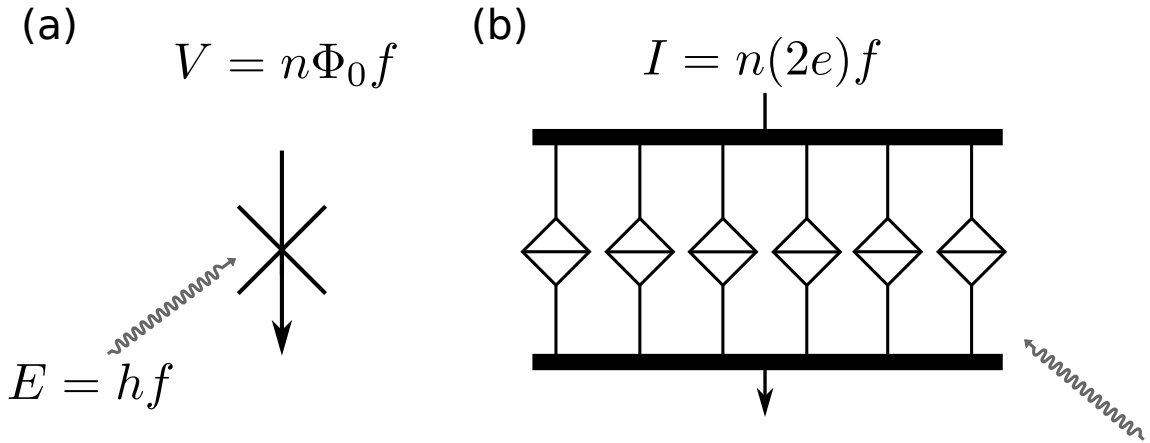


Figure 2.13: (a) Linear Josephson junction array used as a conventional volt definition based on the ability of to act as a perfect frequency-to-voltage converter. (b) Circuit of parallel nanowires acting as QPS junctions as a basis for a possible fundamental standard of current, featuring a dual effect to the Shapiro steps.

Suggested in [5] as an application for the duality between Josephson junctions and QPS junctions is the dual circuit for the linear Josephson junction array: an array of parallel QPS nanowires (Fig. 2.13(b)).

Because of the duality, it is expected to see the dual to Shapiro steps in the current-voltage characteristic of a parallel nanowire-array, locking a frequency f to an applied current I with

$$I = N \cdot 2e \cdot f \quad (2.51)$$

A one-dimensional array of nanowires is built up by parallel nanowires with inductance L and QPS amplitude E_s . Together with horizontal connection bars, closed superconducting loops are created, which can contain a vortex. The total horizontal inductance is L_0 . These bars are too wide to allow phase slips. Arrays of nanowires are research issues on recent studies [46], a schematic is shown in figure 2.14.

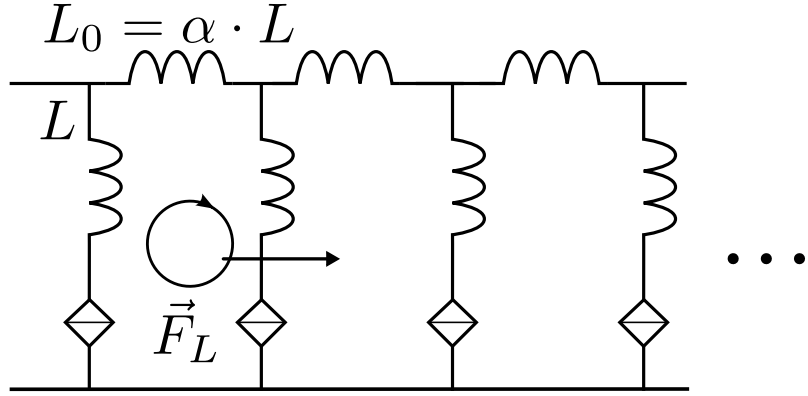


Figure 2.14: The ratio of horizontal and vertical inductance determine the screening length $\lambda_s^f = \sqrt{L/L_0} = \alpha^{-1/2}$ of a fluxoid located in a loop. Fluxoids can be moved through the array, an applied field “pushes” them with the Lorentz force and quantum phase slip processes allow a tunneling through the nanowires.

The phase difference going around one loop has to be 2π periodic and can be described by the vertical phase difference ϕ_i over the nanowire i and the horizontal phase difference η_i . For one loop we find

$$-\phi_i + \eta_i - \phi_{i+1} = (n_i - f) 2\pi \quad (2.52)$$

with n_i , the number of vortices in the loop and $f = \frac{\Phi}{\Phi_0}$ the frustration applied by a magnetic field. For currents we find with $I_i \propto \frac{\phi_i}{L}$ and for zero magnetic field

$$\eta_i = \phi_i - \phi_{i+1} \quad (2.53)$$

Applying Kirchhoff's circuit laws to a current node at the top of wire i we find

$$(\phi_{i+1} - \phi_i) - (\phi_i - \phi_{i-1}) = \frac{L_0}{L} \phi_i = \frac{d}{dx} \phi_i \quad (2.54)$$

with the last equality sign coming from a quasi-continuous approximation. Solving the differential equation we find λ as the characteristic length over which the phase falls off exponentially: the screening length

$$\lambda = \sqrt{\frac{L_0}{L}} = \sqrt{\frac{1}{\alpha}} \quad (2.55)$$

The factor α has no additional meaning, it is only used for convenience to lose the square root and will be used in this thesis to describe the inductance ratio.

Inside an array the fluxoids can be moved due to QPS processes, driven by the Lorentz force of an applied field (Fig. 2.14).

In order to further investigate nanowires as QPS junctions, the goal is to study DC transport measurements on parallel arrays of nanowires via four-point probe measurements with a possible microwave bias.

What is to expect from these measurement? Looking at Josephson junctions, there are some interesting phenomena one can hope to see the dual effect to.

Since the characteristics of the array can be mapped to Josephson junctions, the $I - V$ curves should look similar. The array should show a critical current and ohmic resistance for higher values where superconducting is lost. A hysteresis effect in the down sweep is also expected (Fig. 2.15).

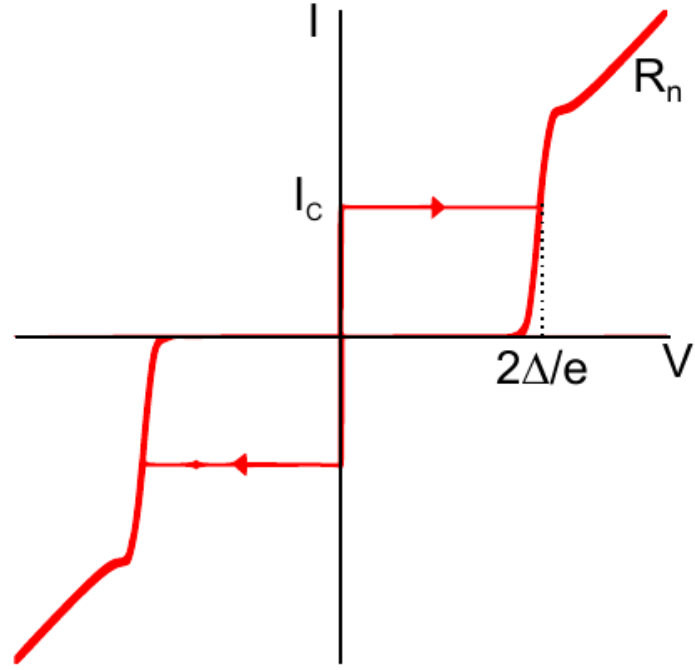


Figure 2.15: (a) $I - V$ curve of a Josephson junction. The junction is superconducting until I_c is reached and then exhibits ohmic behavior. From the hysteresis the gap energy can be calculated. From [47].

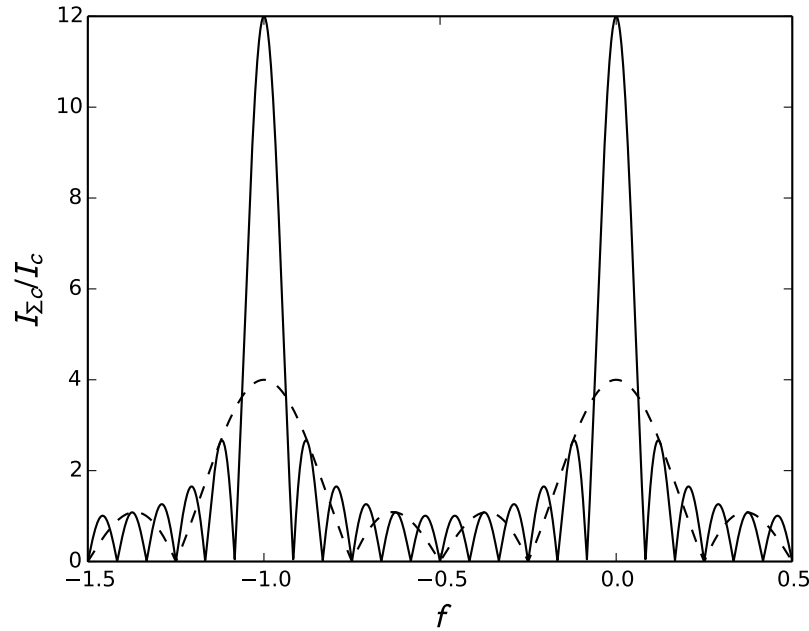


Figure 2.16: The number of junctions can be detected by the Fraunhofer pattern. $I_{\Sigma c}$, the total critical current is plotted versus the frustration coming from the magnetic field. The solid line was simulated for 12 junctions, the dashed line represent 4 junctions.

Josephson junctions exhibit **Fraunhofer diffraction patterns** in the critical current I_c dependent on the magnetic field. A magnetic field is applied parallel to the junction and the critical current shows interference pattern. Mathematically this can be derived by integrating the current density over the junction. This integral has similarities to a

Fourier transform, from which the diffraction pattern can be derived. The observation of the Fraunhofer pattern in a Josephson junction was a prove for the theoretical concept of Cooper pairs tunneling through the barrier [48]. For a linear array of N Josephson junctions the number of junctions can be found in the diffraction pattern. Between principal maxima there are $N - 1$ minima located (Fig. 2.16). A dual effect of the Fraunhofer pattern can be expected in parallel QPS junction arrays as well.

The QPS energy $E_s \propto \exp(R_q/R_\xi)$ was so far considered high in order of QPS. In the opposite case, for $R_\xi \sim R_q$ the quantum fluctuations are strong and the QPS junction should exhibit an insulating state, the **Coulomb blockade**. For a Josephson junction this can be explained by the barrier acting as a capacitor. The electrical current is then suppressed at low bias voltages. The same behavior was found in single QPS junctions [43, 44].

Bloch oscillations, based on the studies by Bloch and Zener [49, 50], are electron oscillations in a crystal lattice coming from a motion in a periodic potential with a constant force. In the original studies seen for electrons in an ion lattice of a crystal oscillating inside the Brillouin zone, Bloch oscillations are now a generalized expression for a quasi-charge in a periodic potential with a constant drive. Such oscillations were predicted [51, 52] for Josephson junctions in the charge regime, with the electric charge being a well defined quantum number. Signatures of these oscillations were found in two peaks for $I = \pm 2e/f$ in a DC differential dV/dI measurement by Kuzmin and Haviland [53]. According to that, Bloch oscillations on QPS junctions with microwave bias could be expected. While Bloch singularities relating current and frequency were observed for a single wire by Lehtinen, Zakharov, and Arutyunov [43], oscillations in voltage have not been observed yet.

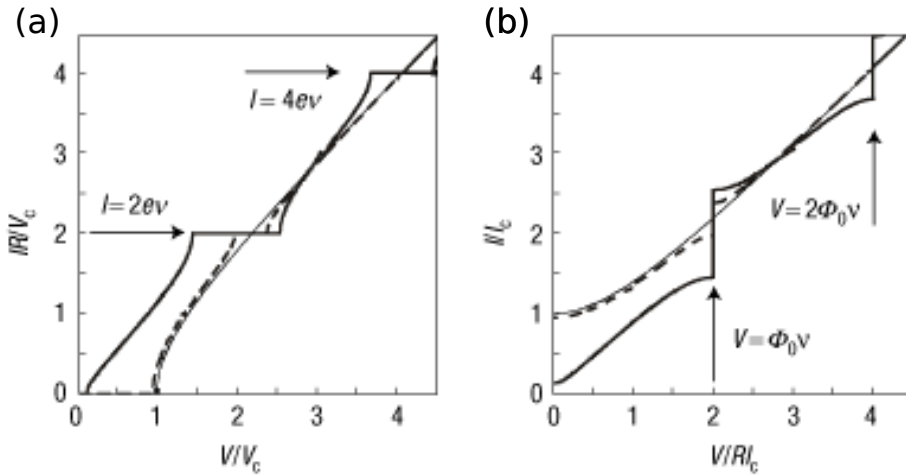


Figure 2.17: (a) Predicted Shapiro steps in a QPS junction with one single wire embedded in a highly resistive environment. (b) Voltage Shapiro steps in the dual circuit simulated for equivalent parameters. From [5].

3 Experimental Details

3.1 Basic idea

The basic design idea for the experiment was a four-point probe measurement with microwave bias on arrays of parallel nanowires. For each experiment, four current leads from a bond pad to the array are needed. A microwave feedline is needed for biasing and has to be coupled to the array leads. These requirements are the same for every experiment. For redundancy reasons and for being able to investigate multiple arrays on one chip several experiments have to be placed on one chip. Putting together all the needed requirements, the fabrication process was separated into two lithography steps. The coarse structures for the wide current leads are defined by optical lithography. They stay the same for every y . The finer structures below $1 \mu\text{m}$ of width are employed via electron-beam lithography. The optical mask contains an experimental space where the array is placed into. Overlap areas connect the two lithography processes. An overview of the whole chip is given in figure 3.1, with the optical part colored in gray and the electron part colored in green.

3.2 Design for a lumped QPS array

Figure 3.2 shows the design of the lumped QPS array. The part for the optical lithography is colored in gray, while the green structures show the electron-beam parts.

In the lumped array case, the characteristic length L of the array is small compared to the size of a fluxoid, which falls off exponentially with λ_s^f . This length is determined by the ratio of the vertical inductance L_v to the horizontal inductance L_h which form the superconducting loops (Sec. 2.5).

$$\lambda_s^f = \sqrt{\frac{L_v}{L_h}} = \sqrt{\frac{1}{\alpha}} \quad (3.1)$$

The kinetic inductance can be expressed using the sheet resistance R_{\square} and critical temperature T_C of the material and the number of squares $N = l/w$ of the structure. The geometric inductance can be neglected at these structural sizes.

$$L_{kin} \propto \frac{NR_n}{T_C} \quad (3.2)$$

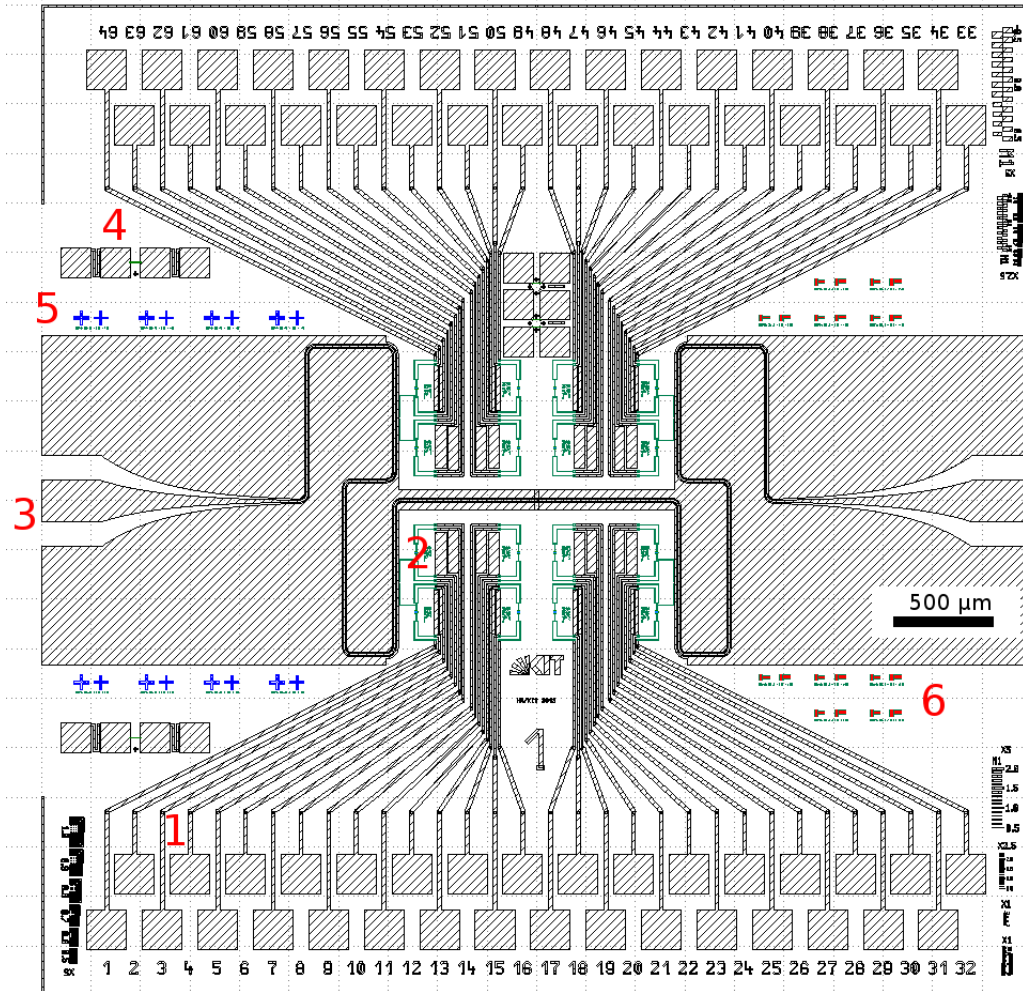


Figure 3.1: The optical design contains bond pads (1) leading to an area containing the actual experiment (2), a microwave feedline (3) and measurement pads for test wires (4). The design for electron beam lithography is already included in this picture. They are shown in more detail in Figs. 3.2 and 3.3. The area dose test patterns (5) and the wire test pattern (6).

Taking a look at α we find, that for an array made out of one single material, R_{\square} and T_C fall out of the ratio. The only parameters are the number of horizontal N_h and vertical squares N_v .

$$\alpha = \frac{N_h}{N_v} \quad (3.3)$$

In the lumped array case, α needs to be small, meaning the number of horizontal squares has to be smaller than the number of vertical squares. The idea for designing the array with a distinct α is, to adapt the width of the upper and lower horizontal bar w_h . For a given wire length l_{wire} and wire pitch p the ration of the number of squares can be tuned. The area of one superconducting loop A determines the flux Φ inside, given a magnetic field B

$$A = \frac{\Phi}{B} \quad (3.4)$$

Since we want to study arrays with different wire length, the loop area would change for different parameters. For convenience purposes, the loop area is kept constant for all

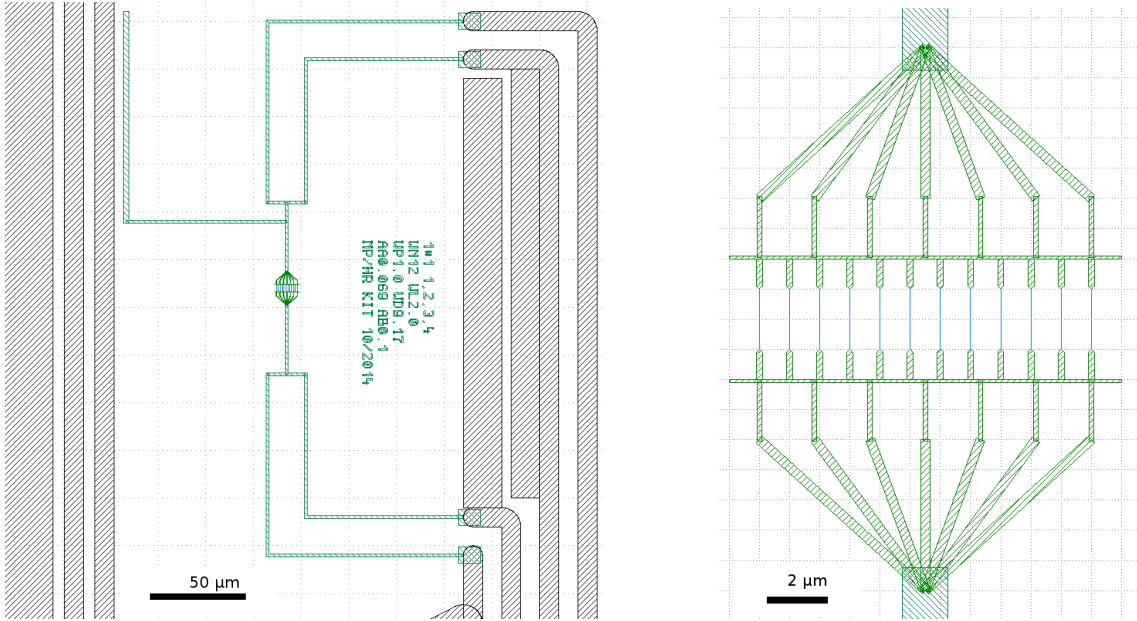


Figure 3.2: The e-beam structures (green) are placed into the experimental space in the optical mask (gray). The coupling to the feedline is designed capacitively in form of an elbow structure, located on the left-hand side of the figure. The lead is split up to distribute the current over the whole length of the array. The figure on the right-hand side is a zoom for a detailed view.

experiments by fixing the pitch of the wires p and the width of the array w_{array} . The array width was fixed by adding vertical leads from the wire ends to the horizontal bars. Putting it all together the w_h can be calculated using

$$\alpha = \frac{N_h}{N_v} \quad (3.5)$$

$$= \frac{l_h/w_h}{l_{lead}/w_{lead} + l_{wire}/w_{wire} + \frac{1}{2}} \quad (3.6)$$

$$\Rightarrow w_h = \frac{1}{\alpha} \cdot \frac{l_h}{l_{lead}/w_{lead} + l_{wire}/w_{wire} + \frac{1}{2}} \quad (3.7)$$

The added $1/2$ in the denominator come from the triangular shapes at the end of the vertical leads, which sum up to be 0.5 squares. The number of wires does not play an important role in the design process, the length of the array is only limited to the size of the experimental space in the optical lithography structure. With the given design and wire lengths of 0.25 to 2.0 μm , α is in a range of $\lesssim 0.1$. Since $\alpha \propto \frac{1}{w_h}$, the width of the bar would reach the fabrication limit of $\sim 100 \text{ nm}$ for higher values of α . The array design is modified to reach flux localization (Fig. 3.3).

3.3 Design for flux localization in the array

Experiments with $\alpha \sim 1$ are very interesting regarding flux localization and fluxoid dynamics, responding to an applied magnetic field. The width of the horizontal bar cannot be reduced any further, so the horizontal connection bars, and therefore the whole array, has to become longer. In order to satisfy the available experimental space and keep the loop size (and therefore the magnetic field) for a fluxoid at a reasonable value, the horizontal connection is formed in a meander-like structure. This approach is shown in figure 3.3. The width of the meander is fixed to 100 nm and the total length of the meander can be

derived from Eq. (3.7). Looking at the current splitting in Fig. 3.2, the current does not get equally distributed. The split wires have different horizontal proportions which leads to lower currents at the ends of the array. This effect can be minimized by adding more vertical inductance after the splitting. To achieve this, it is shifted further away from the array. The area of one loop is not constant anymore, but has to be calculated for the specific design parameters separately.

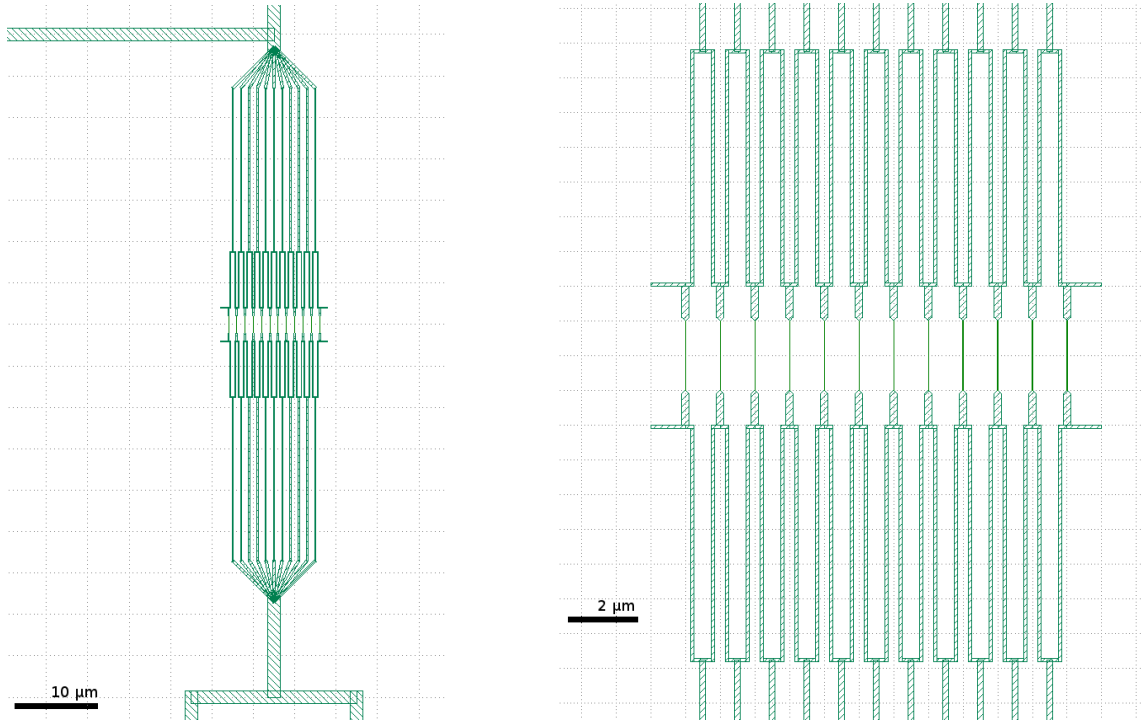


Figure 3.3: For fluxoid localization more horizontal squares are needed. Because of limited space and to obtain reasonable loop sizes, the connections are formed in a meander shape. The current splitting is shifted further away from the array to obtain a more uniform current distribution.

4 Experimental Constraints for QPS

4.1 Materials in QPS studies

How can we influence the QPS rate into an observable range by making good choices for material and wire properties? Taking a look at the QPS rate Γ_{QPS} (Eq. 2.33), the crucial factor is the exponent, containing the quantum resistance R_q , the normal state resistance R_ξ and a constant factor which is neglected here.

$$\begin{aligned}\Gamma_{QPS} &\propto \exp\left(-\frac{R_q}{R_\xi}\right) \\ &= \exp\left(-R_q \cdot \frac{w}{R_\square \cdot \xi}\right)\end{aligned}\quad (4.1)$$

with the sheet resistance R_\square , the wire width w and the coherence length ξ . From this equation the key elements for a high enough R_ξ can be detected.

1. *High sheet resistance R_\square*
2. *Long coherence length ξ or low T_c respectively*

The width is a fabrication factor. For wire dimensions within the fabrication limit (about 15 nm width) we need sufficient high ξ . The longer the coherence length, the wider the wire can be.

$$w \sim \xi \propto \frac{1}{T_c} \quad (4.2)$$

In recent years, lots of studies on QPS effects in nanowires have been published. Numerous materials were investigated for example MoGe [26, 54, 55], InO_x [6], NbN [41], Ti [29, 42, 56] and NbSi [57]. The properties of the studied wires, as well as distinct material parameters are listed in table 4.1. R_\square is the sheet resistance, a is a factor for calculating $L_{kin} = a \frac{\hbar R_n}{\pi \Delta}$, the London penetration depth $\lambda = \sqrt{L_{kin}/\mu_0}$ [18], the energy gap according to BCS Δ and the coherence length ξ .

Observing similarities in these parameters raises the question, if materials with comparable properties can show QPS effects as well.

4.2 Material of choice: granular aluminium

Following the considerations above, we started investigating metallic aluminium-oxide (AlO_x) as a possible material to show QPS effects. Studies in growth conditions and

Table 4.1: Material and nanowire parameters from recent QPS studies. Analog to [18]. The samples investigated in this thesis were fabricated out of metallic aluminium oxide (AlO_x). Its data is listed here as well.

Material	Width (nm)	Height (nm)	Length (μm)	R_{\square} (kΩ)	a	λ (μm)	Δ (meV)	ξ (nm)
InO_x	40	35	0.4	1.7	1.8	6.6	0.41	20
					1	4.9		
NbN	30	3	0.5	2.0	4.8	1.7	1.6	4
					1	0.79		
Ti	24	24	20	1.1	1	8.5	0.06	80
					2	12		
NbSi	20	10	5	0.66	1	2.5	0.18	15
					2	3.5		
AlO_x					1.3	2.2	0.25	10-20

structural properties of thermal evaporated AlO_x films [58] indicate, that the electric sheet resistance can be tuned by the oxygen partial pressure in the growth atmosphere. Starting from this approach, we grow AlO_x films using a reactive DC magnetron sputtering process (Sec. 5.2). Several measurements investigating the sheet resistance, granularity, annealing behavior, kinetic inductance, and measurements of the internal quality factor have been made [59].

4.2.1 Sheet resistance vs Argon pressure

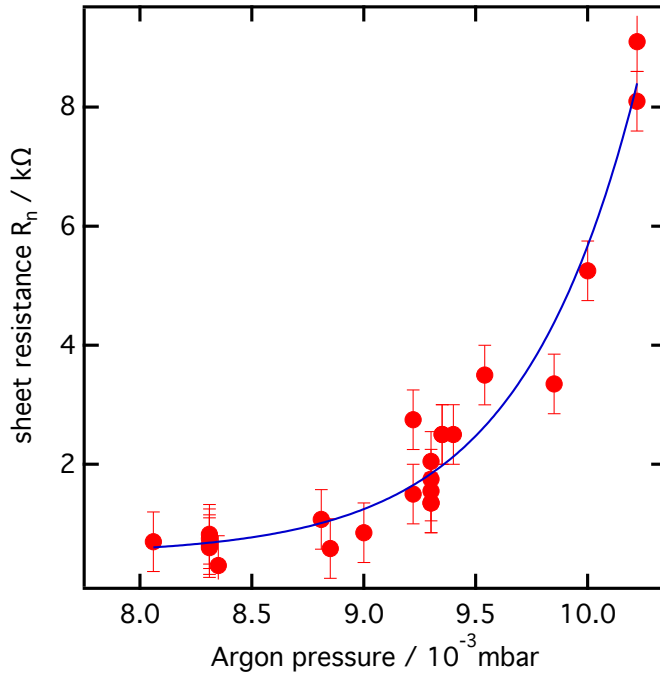


Figure 4.1: The Ar partial pressure is used to tune the sheet resistance of the AlO_x film. The solid line fits the data point to an exponential curve using least square fitting [60].

Reactive sputtering was approached due to the enhanced reproducibility of the sheet resistance compared to thermal evaporation. There, a aluminium source gets heated to melting

temperature and oxygen implantation contaminates the source. During a sputter process the aluminum source stays cold. The atoms are milled out via momentum transfer and the target remains solid. The surface oxides are removed in a pre-sputter process with pure Ar plasma. The actual sputter process is done by leading an Ar/O₂ 9:1 mixture via a mass flow controller into the main chamber. The film growth rate and the oxygen partial pressure determine the total amount of implanted oxygen, and therefore the sheet resistance. By leaving the O₂ partial pressure constant and using the partial pressure of the pure Ar gas as a reference, the sheet resistance can be tuned. The films were deposited aiming at a sheet resistance value range from 0.1 to 10 kΩ to get a sufficiently high QPS rate and study superconductor-insulator transition by using thermal annealing to tune the material parameters after deposition. The film was deposited with a thickness of 20 nm. Using that technique, the parameter variations were less than 2 nm in thickness and with a R_{\square} accuracy of ± 0.5 kΩ [59].

4.2.2 Temperature dependence of the granular structure

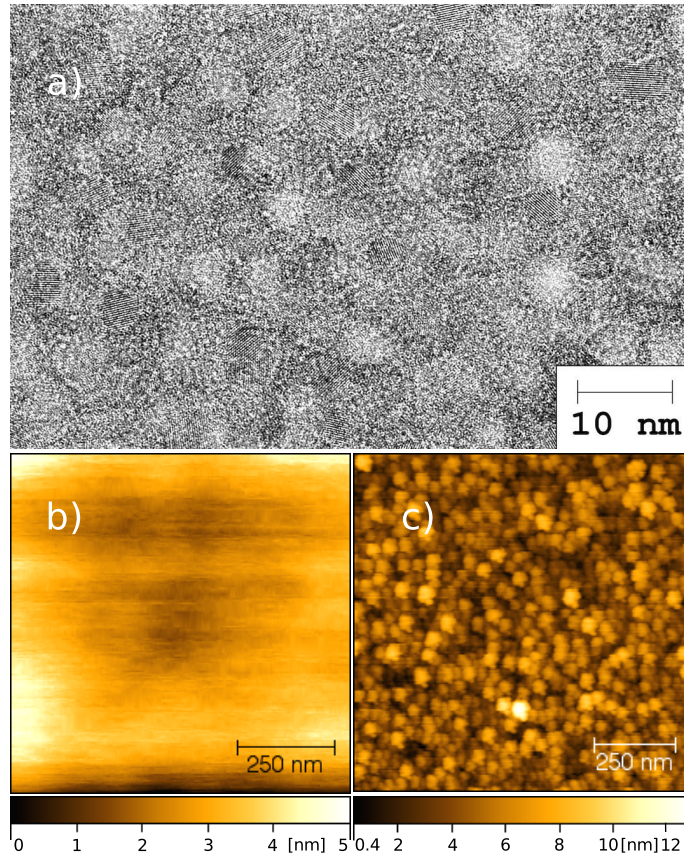


Figure 4.2: The TEM image (a) shows an un-annealed AlO_x film. The mean grain size is about 4 nm. The AFM pictures show a film before (b) and after (c) annealing for 600 s at 250 °C. While clearly visible in the annealed film, the grains are not distinguishable in the original film. Note the different scale. [59]

The granularity of the material was investigated using transmission electron microscopy (TEM). A TEM image for a film with a $R_{\square} \sim 2$ kΩ is shown in figure 4.2(a). The visible granular structure contains 4 nm aluminium grains embedded in a oxygen-matrix. This is important for experiments with nanowires, since the wire dimensions cannot reach the limit of the grain size. Looking at the grains with an atomic force microscope (AFM) before (b) and after (c) thermal treatment indicates a growth of the grains to ~ 22 nm. Heat treatment of films is used as a method of tuning sample parameters after the fabri-

cation. On the other hand is some heat treatment unavoidable during thin film patterning processes. The influence of temperature on the resistance was studied by annealing AlO_x films on a hotplate. The resistance decreases within seconds, before entering a plateau value after several minutes. This decrease may be due to the growing Al grains, leading to a longer electron mean free path. In figure 4.3(a) the normal sheet resistance is plotted versus the annealing temperature. A insulator-superconductor transition by an annealing of the sheet resistance below the quantum resistance R_q can also be observed (Fig. 4.3(b)). The ratio RRR of the sheet resistance at room temperature R_n (300 K) to the sheet resistance R_n can be determined to $RRR = 1.3$.

For temperatures below 200 °C, the sheet resistance changes only about 10 %, which makes the AlO_x suitable for patterning processes.

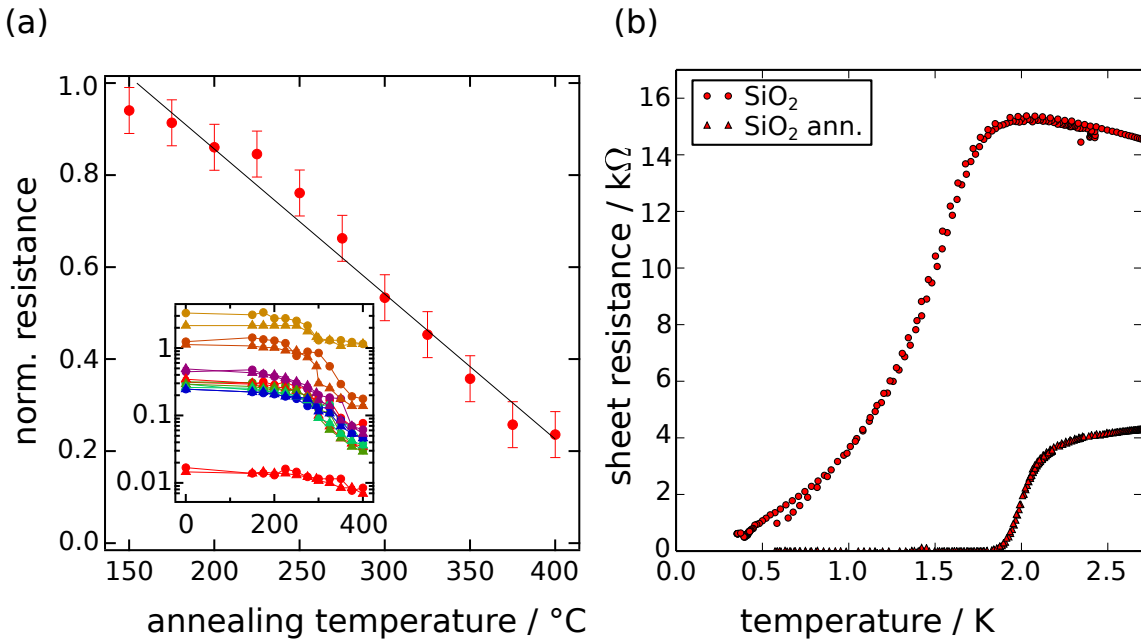


Figure 4.3: (a) The normalized sheet resistance $R(T)/R(300 \text{ K})$ shows a universal behavior between 200 and 400 °C for R_n below $\sim 20 \text{ k}\Omega$. In the inset, the individual films are shown. Note the logarithmic scale. From [59]. (b) Resistance measurement for a sample before and after annealing. The sheet resistance is annealed below the quantum resistance and the film gets superconducting. From [61].

4.2.3 Microwave properties

The microwave properties of the AlO_x films were studied using transmission measurements of feed line coupled, $\lambda/4$ coplanar waveguide resonators (CPW). The internal quality factor, a parameter describing the energy loss due to internal dissipation, was measured up to 674 000 at a power level of -100 dBm . In table 4.2, the quality factors for different power levels are listed. Figure 4.4 shows a typical transmission measurement at -90 dBm power.

Table 4.2: Internal quality factor Q_i measured with a $\lambda/4$ resonator out of AlO_x at different power levels at a resonance frequency $\omega_0 = 4.04 \text{ GHz}$ [59]

Power / dBm	-80	-90	-100	-115	-130
$Q_i / 10^3$	343	668	674	329	126

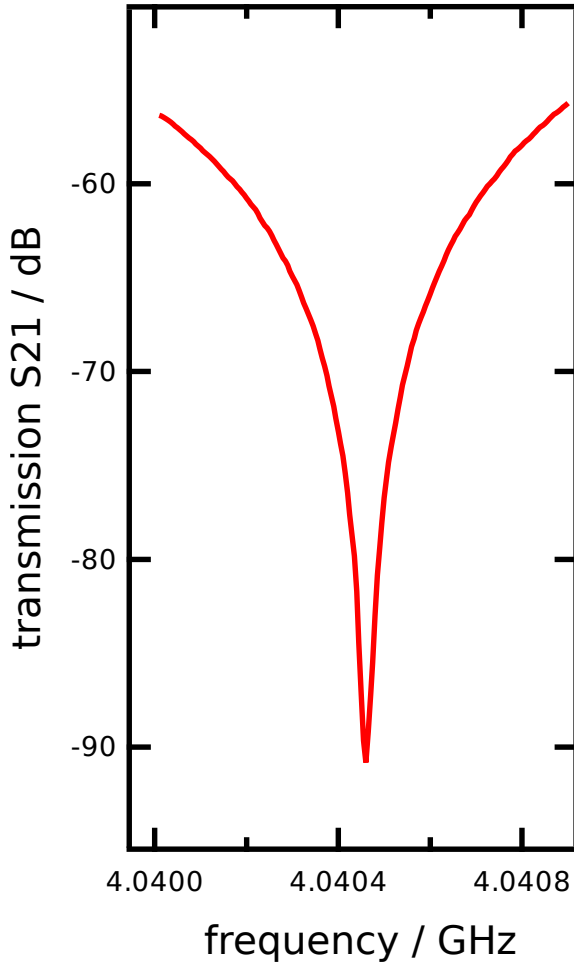


Figure 4.4: Microwave transmission measurement for a $\lambda/4$ resonator at -90 dBm power level showing a internal quality factor of 668 000 [59].

Transmission measurements on a $\lambda/2$ resonator before and after annealing were used to evaluate the formula for the kinetic sheet inductance

$$L_{kin} = 0.18 \frac{\hbar R_n}{k_B T_c} \quad (4.3)$$

For a $\lambda/2$ CPW resonator, the resonance frequency of the integer harmonic n is given by

$$f_n = \frac{n}{2l} \sqrt{\frac{1}{LC}} \quad (4.4)$$

The total inductance $L = L_{geo} + g_{kin}L_{kin}$ consists of the geometric inductance L_{geo} and the kinetic inductance L_{kin} . With the length l and the total number of squares N it follows

$$g_{kin} = \alpha \frac{N}{l} = \frac{\alpha}{w} \quad (4.5)$$

$$\alpha = \frac{w}{L_{kin}} \left[\left((2f_0 l)^2 C \right)^{-1} - L_{geo} \right] \quad (4.6)$$

By measuring the sample, the fundamental mode $f_0 = f_n - f_{n-1}$ could be determined. The kinetic inductance is calculated using equation 4.3. We find $\alpha = 0.96$ (non-annealed) and

$\alpha = 0.86$ (annealed). This allows to estimate the base frequency of an annealed resonator by a sheet resistance measurement and the data confirm equation 4.3. Comparing this with the calculations done in [18], the approach for the kinetic inductance there features an estimated parameter a

$$L_{kin} = a \frac{\hbar R_n}{\pi \Delta} = \frac{a}{\pi \cdot 1.78} \frac{\hbar R_n}{k_B T_c} \quad (4.7)$$

Calculating this factor from the measured data, delivers $a = 1.3$, valid for R_n near T_c . For room temperature measurements of the sheet resistance R_n (300 K) we get $a = 1$.

Material conclusion

AlO_x is a high kinetic inductance material with good microwave properties. The films can be easily fabricated and show only little aging effect, while being stored at ambient room temperature. Reactive sputter deposition delivers reproducible sheet resistance in a wide range, which can be tuned afterwards by thermal annealing. The critical temperature is not influenced by temperature. The material can be used to perform standard microfabrication processes, for temperatures under 200 °C the sheet resistance changes only very little.

Table 4.3: Material parameters for granular aluminium.

$R_n(300 \text{ K})$ ($\text{k}\Omega$)	RRR	a	λ (μm)	Δ (meV)	ξ (nm)
~ 1	1.3	1.3	2.2	0.25	10-20

Putting all the information together, allows the comparison of the AlO_x parameters to those of different QPS materials (see table 4.1).

The AlO_x shares similar material properties with these materials. With this comparison, it is reasonable to expect QPS effects, if observable in AlO_x , in nanowires of the same dimensions like in the studies listed above.

5 Sample Preparation

5.1 Basic fabrication concept

The samples are fabricated using a SiO_2 passivated $20 \times 20 \text{ mm}^2$ Si substrate. The chip is cleaned in-situ from water and organic residue using an argon plasma, before a thin film of metallic aluminium-oxide (AlO_x) in the range of 20 nm with a sheet resistance of about $1 \text{ k}\Omega$ is deposited. Via thermal evaporation, a thin niobium layer is added. It oxidizes completely and serves as an etch protection layer for the AlO_x . The sample undergoes an electron beam lithography step for the fine structures, positive optical lithography defines the coarse structures. The patterns in the resists are transferred into the AlO_x using a Cl^- -based reactive ion etching. There is no etching step between the two lithography processes. A detailed overview of the used fabrication parameters, as well as additional remarks and suggestions is given in appendix A.

5.2 Sputter deposition

The AlO_x film is applied using DC magnetron sputter deposition. The sample is cleaned from water and organics in-situ by an Ar plasma in the load lock, before being transferred into the main chamber. By applying a high DC voltage to the aluminium target, the inserted argon gas in the chamber gets ionized and a plasma is ignited. The ions hit the target surface and aluminium atoms are milled out. Together with the oxygen in the main chamber atmosphere, the particles redeposit as a granular aluminium-oxide film on the sample. The sheet resistance depends on the amount of oxygen implanted into the film. Since the sputter target and the sample are not arranged symmetrically, the sample holder in the main chamber is rotated during the sputter process. The gases are inserted into the chamber using independent mass flow controllers for the pure Ar gas and the Ar/ O_2 mixture. Figure 5.1 shows a schematic overview of the deposition tool.

The goal were AlO_x films with a thickness of 20 nm and a sheet resistance of $1 \text{ k}\Omega/\square$. Using this process, these target values could be reached with an uncertainty of $\pm 2 \text{ nm}$ and better than $\pm 0.5 \text{ k}\Omega/\square$ (Sec. 4.2.1).

5.3 Thermal evaporation

In addition to the sputtered AlO_x , a layer of niobium is evaporated on the chip. The layer is deposited slowly and very thin, so effectively oxidized niobium is applied. The Nb is

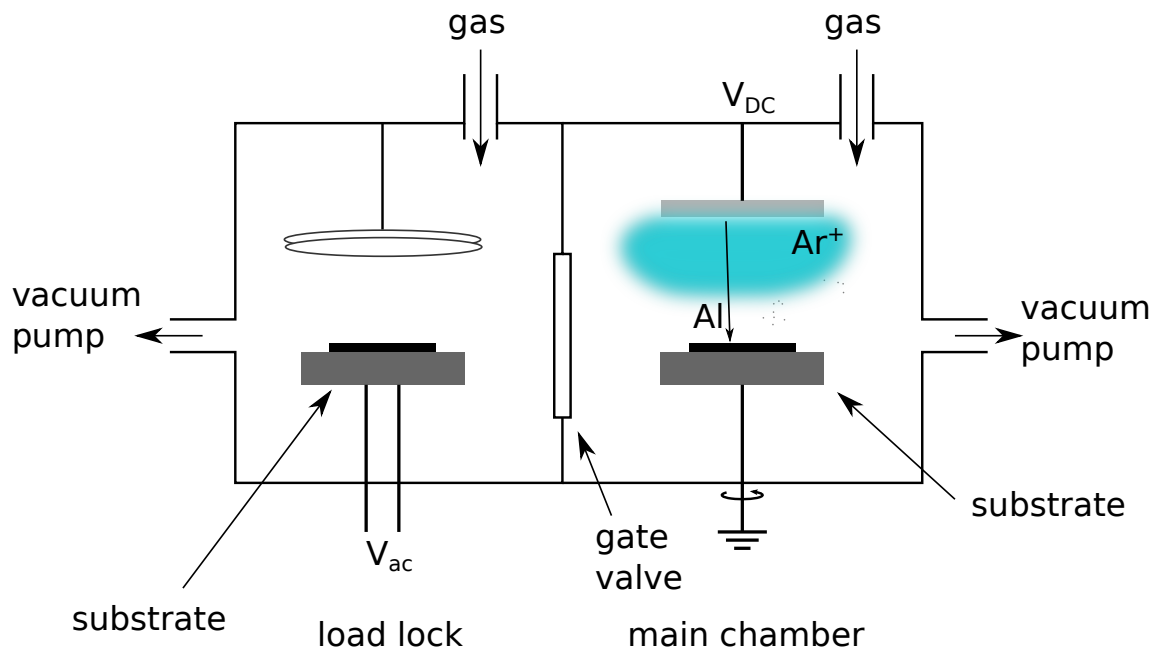


Figure 5.1: Schematic overview of the DC magnetron sputter tool. An Ar plasma in the load lock is used to clean the chip from water and organics. The plasma in the main chamber mills aluminium atoms out of the target. Together with the oxygen in the main chamber atmosphere they form our AlO_x film.

used as an etch stop layer to protect the AlO_x from chemical developer used in further fabrication processes (Sec. 5.4). It can withstand the base on a timescale sufficient long enough for our development processes. The added layer does change the resistance of the system only in the order of $10\ \Omega$, which is negligible for our films.

The niobium is deposited by thermal evaporation in a *PLASSYS MEB 550s* shadow evaporator. It is a two chamber system with the load lock located above the main chamber. The crucibles filled with the evaporation material are located at the bottom of the main chamber in a high vacuum environment created by a cryogenic pump. An electron beam is focused on the material, causing it to sublime. The gaseous atoms condense on the chip forming a metallic layer. For the deposition of the niobium, the evaporation system is operated in manual control. A detailed description of the manual evaporation can be found in appendix B. Figure 5.2 shows a schematic overview of the evaporation machine.

5.4 Lithography

Lithography processes are used in microfabrication to structure a defined pattern onto substrates. Both lithography steps, electron beam lithography and optical lithography, used in the fabrication process share the same principle. Resist, a chemical sensitive to a certain type of exposure is applied on the chip surface. It gets exposed to either electrons or UV-light, changing the chemical properties of the applied resist. Depending on the process the resist gets either soluble or insoluble to a development chemical. A writing pattern (e-beam) or an optical mask (optical) containing the structuring information is used to expose the resist only at specific points (see figures in chapter 3). The exposure is done using a *SUSS MicroTech Karl Suss MA6* mask aligner containing a mercury-vapor lamp filtered to the 365 nm wavelength I-line. The chip is placed under a chromium mask containing the pattern and precisely positioned using a microscope and a manual positioning system. For the exposure, the mask and the chip are brought in direct contact to avoid interference effects. The light intensity and the exposure time determine the accuracy of the transferred pattern.

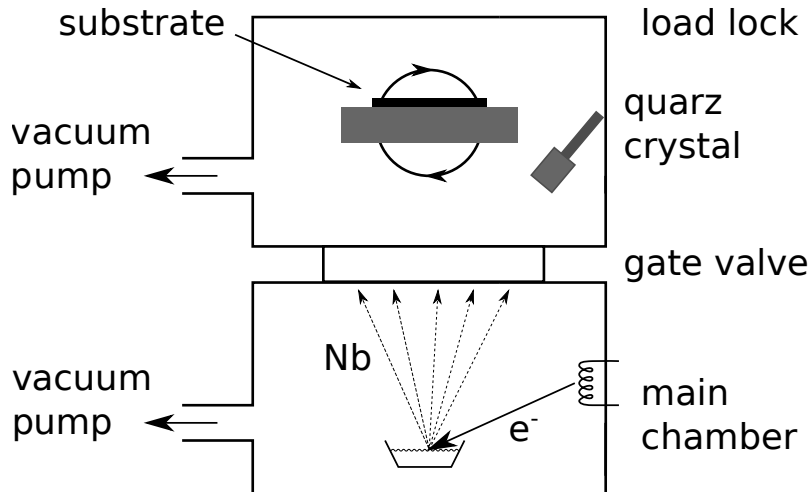


Figure 5.2: Schematic overview of the thermal evaporation tool *PLASSYS MEB 550s*. The load lock on top features a quartz crystal for measuring the film thickness and a rotatable sample holder. In the main chamber, an electron beam is focused on a crucible containing the evaporation material, causing it to sublime. The material redeposits on the chip surface.

5.5 Reactive ion etching

After the lithography steps, the defined structures are only present in the resists. As final fabrication step an etching process is mandatory to transfer the patterns into the AlO_x beneath. For this step, we perform a dry-etching process with a *Oxford Plasmalab100 ICP* etching machine. The plasma is created by impact ionization and is directed to the chip surface. The Cl^- -ions attack the AlO_x layer to form gaseous AlCl_3 , which gets pumped away from the chip surface. Due to the high acceleration power, the Ar ions in the plasma perform a physical etching process by milling, material-independently, atoms out of the surface. Therefore, the HSQ etch mask gets also attacked.

The process parameters were determined by measuring the etching rates of the used materials. The goal was a process which transfers the resist pattern into the metal on a timescale long enough to create reproducible results. The rates were determined by putting a thin cover glass over a sample to etch an edge into the substrate. The edges were measured using a *Nanosurf easyScan 2 FlexAFM*.

5.6 Fabrication results

5.6.1 Electron-beam parameters

The essential writing parameter for e-beam lithography is the deposited dose, determining the amount of energy transferred into the resist. Area-dose test patterns were investigated to determine the correct dose for the coarse structures. The test patterns were investigated using a *Zeiss Supra 55VP SmartSEM*.

The dose values refers to infinite planes, since every electron shot influences the resist next to it by scattering. The lithography system considers this for finite structures by adapting the dose on edges and corners. However, the interaction of the beam electrons with the resist and substrate leads to a non-zero dose in areas outside the writing pattern, the proximity effect. The proximity effect is described by the point spread function.

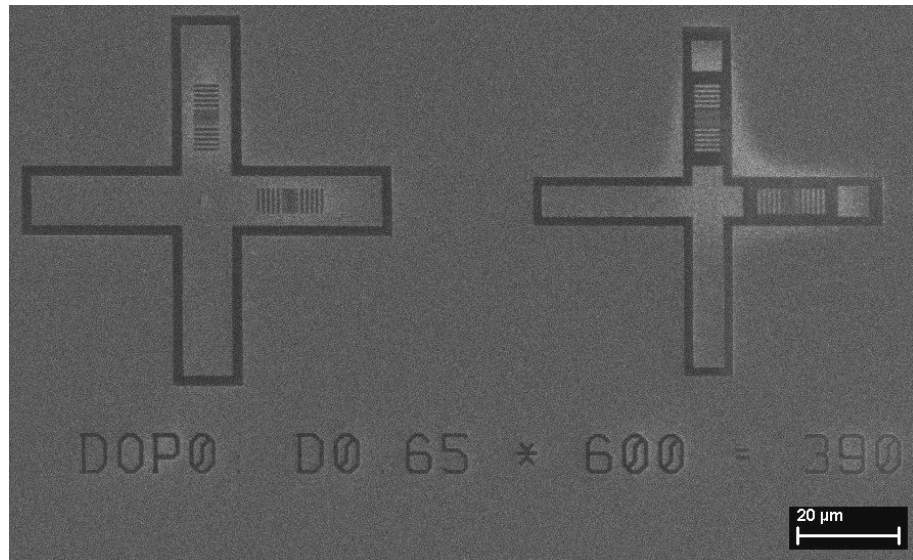


Figure 5.3: Area-dose test pattern to determine the best doses for the e-beam lithography. The latest results show, that the dose should be reduced further to $390 \mu\text{C}/\text{cm}^2$.

Using a two-Gaussian model for forward scattering and backscattering, a three-dimensional diffraction pattern of electrons emitted from an infinitely small point source is described.

$$PSF = \frac{1}{\pi(1+\eta)} \left[\frac{1}{\alpha^2} e^{-\frac{r^2}{\alpha^2}} + \frac{\eta}{\beta^2} e^{-\frac{r^2}{\beta^2}} \right] \quad (5.1)$$

with α and β describing the forward and backward scattering, while η describes the contribution of the back scattered electrons. The parameters depend on the used resist and substrate materials. The were estimated by a Monte Carlo simulation, using *NEA-1525 PENELOPE2011*¹. The simulation resulted in $\alpha = 0.002205 \mu\text{m}$, $\beta = 8.958633 \mu\text{m}$ and $\eta = 0.798738$ were simulated. The resulting parameters are used by the e-beam writer to reduce the proximity effect.

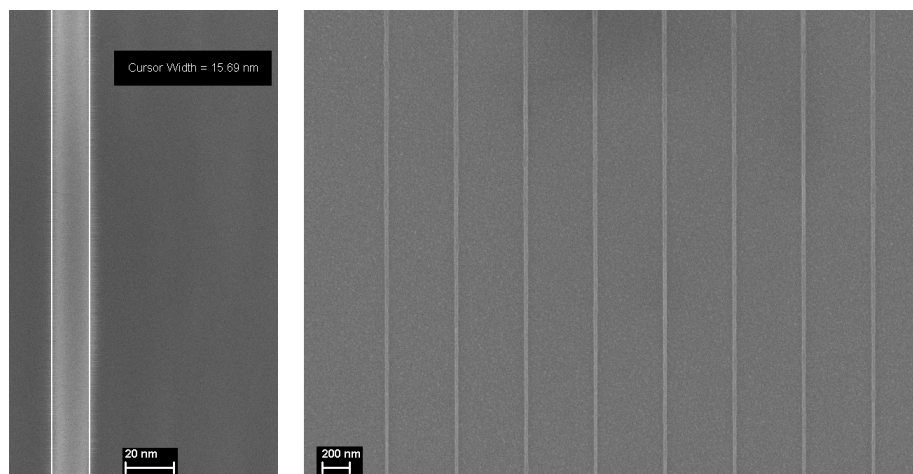


Figure 5.4: (a) Zoom in thinnest single wire. (b) Wire-dose test pattern. The wire width depending on the writing dose was evaluated and $5500 \mu\text{C}/\text{cm}^2$ was found as a dose value which produces 25 nm wide wires. With lower doses even thinner wires could be fabricated.

¹<http://www.oecd-nea.org/tools/abstract/detail/nea-1525>

The writing dose is used to adjust the width of the nanowires, while the lithography machine writes the thinnest line possible. The electrons are scattered from the point of entry and the width of the exposed resist is wider than the written line. By writing test patterns with different doses, the dose value resulting in a width of about 25 nm was determined. By using the writing dose as a parameter for the width of the nanowires, nanowires even smaller than 15 nm could be reached. Increasing the doses, wider and more robust wires could be observed. Figures 5.4 show SEM pictures of nanowires.

5.6.2 Connecting e-beam with optical lithography

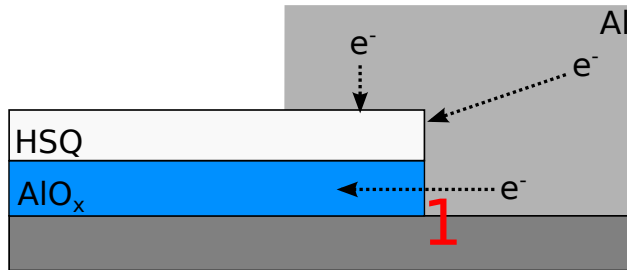


Figure 5.5: Using the HSQ as etch mask in the first lithography process can create contact problems to the possible second metallic layer. Only at the vertical contact area (1) a current flow might be possible. It is not clear how good the Al would be deposited into this corner. Together with a possible undercut in the AlO_x from the etching, this method is not suitable for good reproducibility.

Applying the optical resist onto the structured e-beam resist is an unusual and non-trivial fabrication step. Usually, each lithography step has its own etching process. In this system, it is not that easy to divide the etching process. Galvanic contact through the whole system is needed to perform transport measurements. The main issue to overcome is the HSQ resist for the electron beam lithography, which is used because of its very high resolution feature sizes. This resolution can only be reached if the HSQ is used as an etch mask, being it on top of everything e-beam written. Exposed HSQ can be regarded similar to SiO_2 , making it hard to remove after a possible AlO_x etching step without attacking the metal layer below. Performing the e-beam lithography as a second step is also not ideal, the HSQ thickness of only about 80 nm can cause significant step coverage problems. For better understanding, the problem is illustrated in figure 5.5.

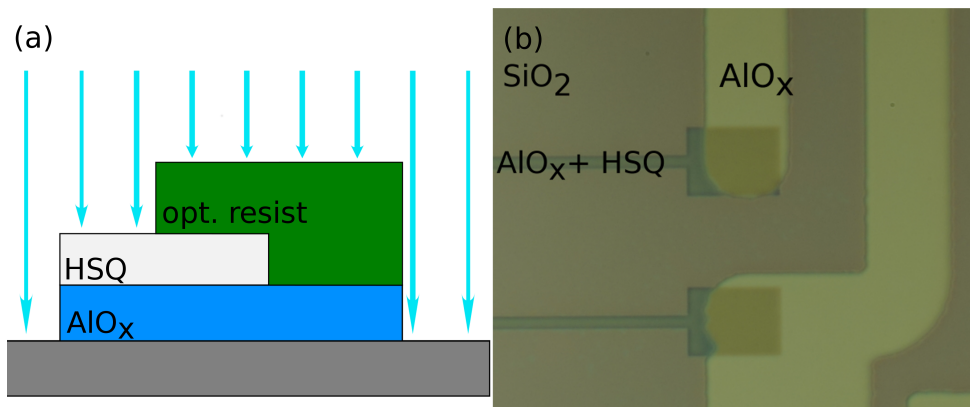


Figure 5.6: (a) Resulting scheme for connecting the two lithography steps. To avoid contact problems, the resists overlap and a continuous metallic layer is defined. The HSQ does not get effected by the second development step, at least on the time scale here. (b) Optical picture of the etched contact pads after removing the optical resist. The HSQ remains on the e-beam structures. This can be seen by the different colors in the picture.

5.6 Fabrication results

The final approach was, to etch e-beam and optical part together in one step. The contact problem would be solved since the resists would overlap, creating one single metallic layer. For this to work, the HSQ structures must not get influenced by the second development process. The same developer is used for both resists and it is likely for the HSQ to get in contact with the developer for a second time in the order of about 5 to 10 s. It turns out that written HSQ structures do not change by an “over development” on that time scale. The combination of the two lithography steps without etching in between is a valid fabrication process for our purposes.

6 Experimental Setup

6.1 The Cryostat

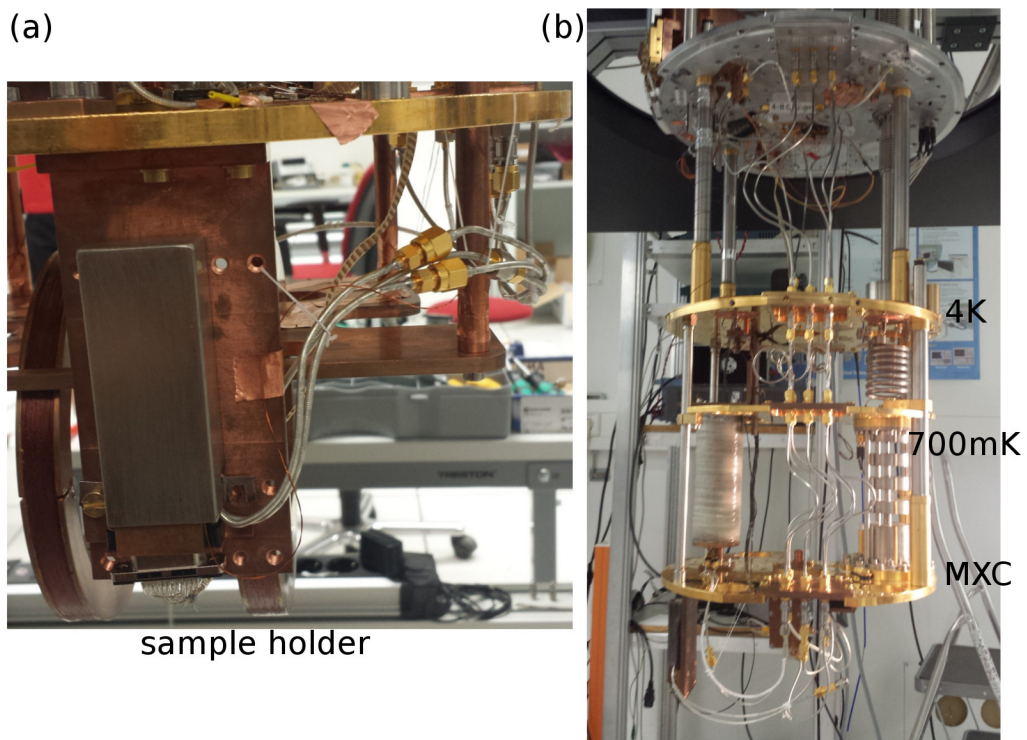


Figure 6.1: (a) The sample holder is connected to the mixing chamber of the dilution refrigerator by a copper holder. The 25 micro sub-D serves as DC lines. (b) Opened fridge. Different temperature stages are shown, the sample holder can be seen in the lower left hand side below the mixing chamber stage.

The samples were investigated using a dry *Bluefors BF-LD-250* dilution refrigerator. The cryostat has several temperature stages reaching a base temperature at the mixing chamber (MXC) of about 20 mK. It is pre-cooled down to 3.6 K by a *Cryomech* pulse tube cooler. The cooling cycle employs the enthalpy of a $^3\text{He}/^4\text{He}$ cooling cycle as outlined below. Milli-Kelvin temperatures are reached by the enthalpy of mixing, using a $^3\text{He}/^4\text{He}$ mixture. The mixture undergoes a phase separation, forming a concentrated phase (^3He -rich) and

a dilute phase (${}^3\text{He}$ -poor). At base temperature the dilute phase consists of $\sim 6.5\%$ ${}^3\text{He}$ and $\sim 93.5\%$ ${}^4\text{He}$, while the concentrated phase is basically pure ${}^3\text{He}$ [62]. The phases are in equilibrium. By bringing the mixture to a non-equilibrium state evaporation cooling takes place. The cryostat inset can be seen in figure 6.1.

6.2 Measurement setup

The measurement setup consists of two current sources. One is used for biasing the four-point probe, the other one for the current supply of the sample holder coil.

The signal from a digital-to-analog converter (DAC) is low pass filtered and supplied to the current source. The current to the sample is again filtered at 300 K with a π -type filter, containing two capacitors and an inductor, inside the vacuum vessel, acting as a low pass. At the 4 K stage a RCR filter reduces again high frequencies from the signal. All measurement wires pass these filters and are additionally coated with copper powder. The copper powder acts as a third low pass filter, due to eddy currents induced at GHz frequencies in the metal. For better handling, the wires are packed together in a 24 line braid and end in a 25 micro sub-D plug connected to the sample holder (section 6.3). The current supply for the magnetic field is π filtered at 300 K, but not at low temperatures.

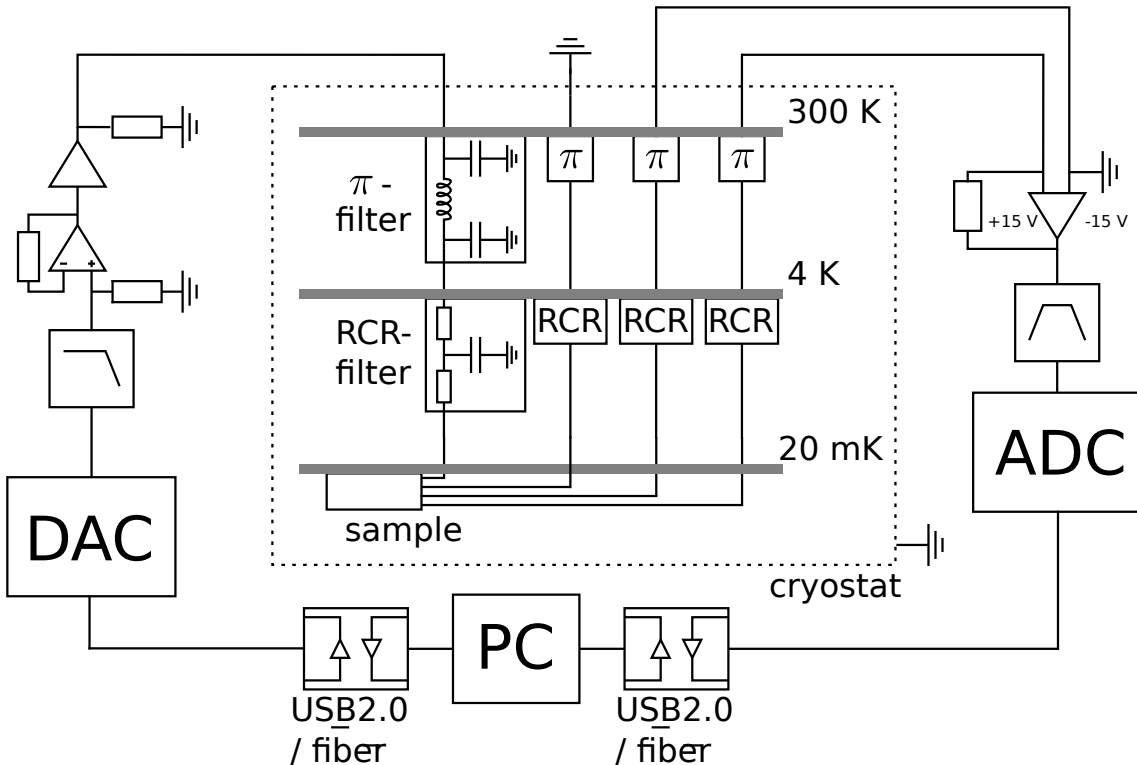


Figure 6.2: Wiring scheme of the measurements. Proper filtering with low passes, π filters, RCR filters, as well as proper grounding is important for a good signal-to-noise ratio. The cryostat mass acts as common ground for all measurement devices, while the measurement computer is galvanic disconnected. A fiber is used for data transfer. Current sources and operational amplifiers operate the four-point probe measurements and the coil current for the magnetic field. Four lines for one measurement are shown here. There are 24 measurement lines leading to the sample holder overall.

Proper grounding is key to avoid interference with the 50 Hz coming from the mains. All the measurement devices share a common ground with the cryostat. A USB2.0-fiber isolator adapter is used to separate the ground from the measurement computer from the experimental setup. In addition, the temperature controller from the cryostat was checked to reduce noise interference.

6.3 Sample Holder

The sample holder used for the measurements is shown in figure 6.3. It is made out of copper, hermetically closed, and suitable for microwave, as well as DC measurements. A Pb shield is placed around the copper box to shield the sample from magnetic stray field.

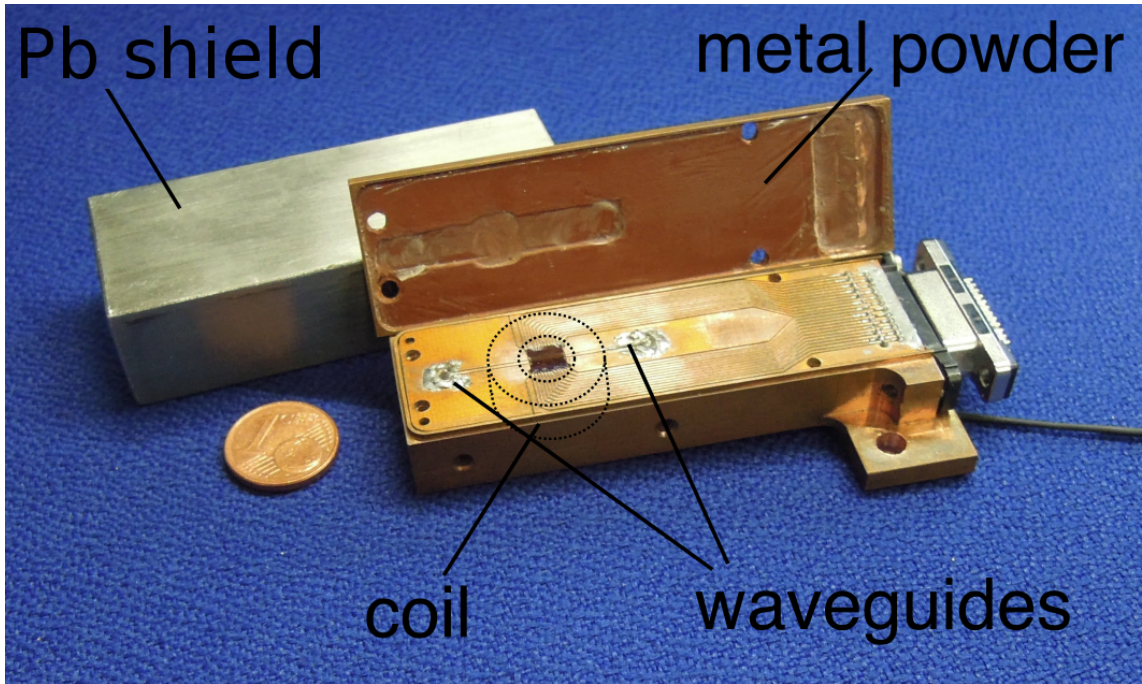


Figure 6.3: The sample holder features a coil placed beneath the sample. A Pb shield is used to protect the experiment from magnetic stray. The inside of the sample holder is coated with metal powder for the same reason. A more detailed picture of the used PCB can be found in figure 6.4.

The printed circuit board (PCB) contains the sample itself and is mounted on top of the copper box. It contains 24 lines for DC measurements, for example six four-point probe measurements, leading to a 25-pin micro D-sub connector. Two mini coaxial connections enable microwave measurements. The metal powder on top of the PCB circuit prevent resonances in the GHz range measured up to 20 GHz.

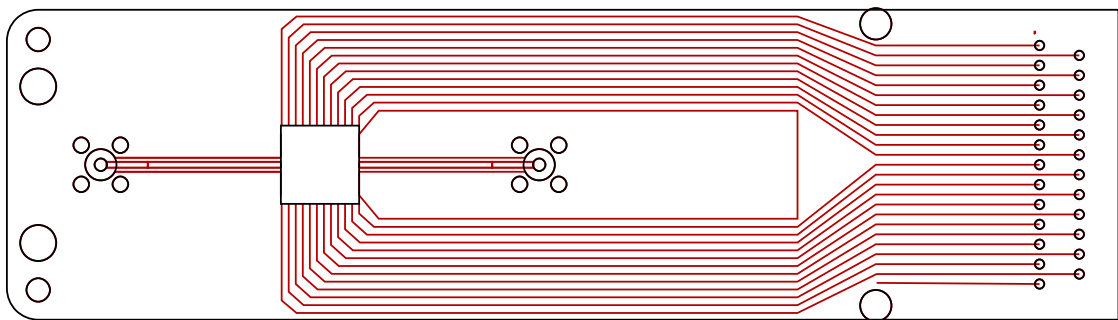


Figure 6.4: PCB used for the measurements.

Inside the sample holder there is a 1024 turn coil made from NbTi in a copper matrix, located right beneath the sample, tested up to $I_B = 80 \text{ mA}$ without heating the cryostat. The magnetic field was measured to be 30 mT/A . This was determined using a the diffraction pattern of a parallel array of Josephson junctions (see [63] for reference)

7 Experimental Results

Two parallel arrays of superconducting nanowires made from AlO_x with different wire length were investigated in this thesis. Both arrays feature 12 parallel nanowires with a nominal width of about 25 nm, connected by a wider segment at the top and bottom of the superconducting wires. The arrays were designed to be in a lumped element limit, the characteristic length of the array is small compared to the size of a fluxoid. As lined out in section 2.5, this can be expressed by the ratio of horizontal inductance from the connecting bars, to the vertical inductance dominated by the nanowires, $\alpha = \frac{L_h}{L_v} = \frac{1}{10}$. The samples were fabricated out of an AlO_x film with a sheet resistance R_{\square} (300 K) $\approx 1 \text{ k}\Omega$. The arrays have a wire length of 0.75 μm and 1.0 μm . For both samples, the $I - V$ characteristics with a current bias and magnetic field dependence were measured. Also, measurements under a voltage biasing scheme were performed.

7.1 Parallel array with 1 μm -nanowires

7.1.1 Current bias

The sample was measured by ramping the bias current in low μA range, creating a mV response. There was no magnetic field applied.

Superconducting behavior up to a critical current I_c of about 1.0 μA is observed, the curve then features a discontinuity in the voltage, continuing at about 4.7 mV. The sample exhibits a step-like structure: A slope with a linear increase in the voltage is followed by a discontinuity in the voltage, leading to higher values. Current plateaus with voltage discontinuities are formed. In the up sweep data, 10 plateaus can be found before the current direction is reversed. The down sweep shows a similar step structure. The hysteresis in the system can be observed, with the curve of the down sweep located below the up sweep curve. For currents below I_c the system does not get superconducting immediately, there is still a voltage measured. The sample gets superconducting again at about 0.45 μA , nearly half the value of the critical current. All plots feature a small offset voltage, due to an offset in the operational amplifier.

The current values of the plateaus in the up sweep are plotted against the corresponding number of plateau in Fig. 7.2(a), showing an almost linear dependence. A similar behavior can be found for the voltage and the power (Figs. 7.2(b) and 7.2(c)). For the voltage dependence the last voltage value for each plateau was plotted against the corresponding number. The power was calculated using the current and voltage values. The dissipation power is in the range of few nW, a rather high value for experiments at mK temperatures.

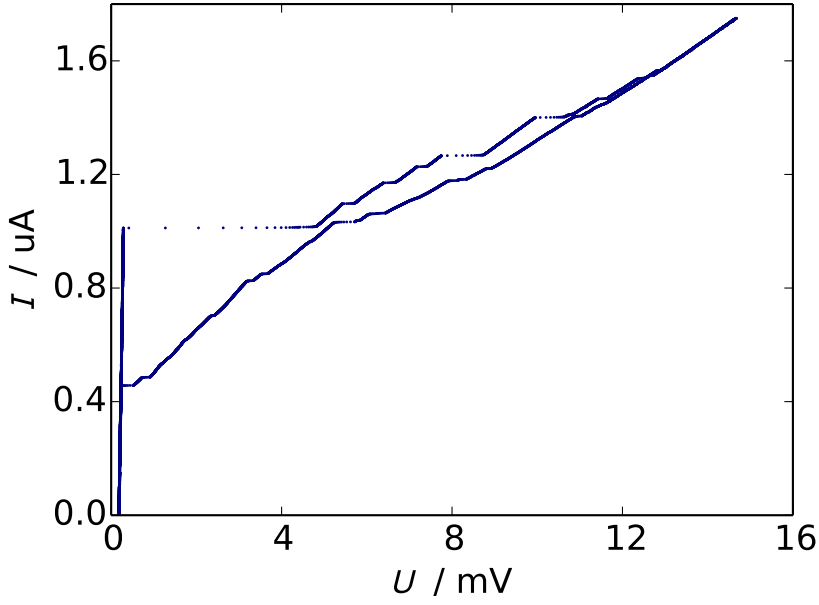


Figure 7.1: $I - V$ curve, current biased for zero field. The current is ramped in low μA range. The sample features a superconducting behavior, up to a critical current, followed by a step structure featuring current plateaus and an ohmic behavior. The steps are repeated in the down sweep.

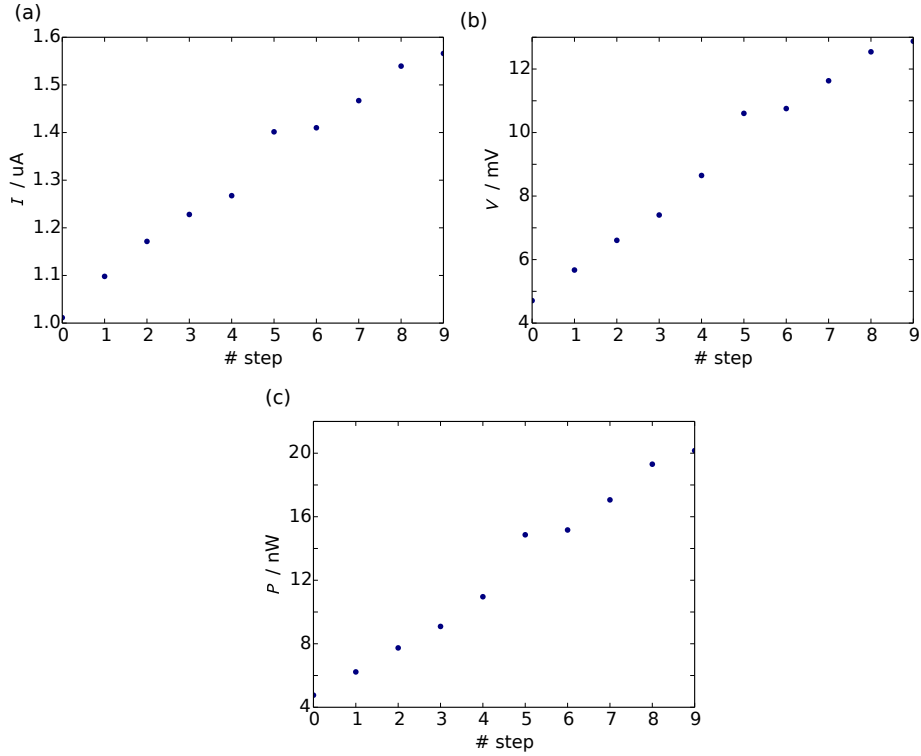


Figure 7.2: (a) Current on plateau versus number of plateau. (b) Last voltage value of plateau versus number of plateau. (b) Dissipated power $P = U \cdot I$ versus number of plateau.

The slopes connecting the different plateaus feature a linear current-voltage dependence and were fitted into lines using the data from the up sweep. The gradient of each fit

represents a constant resistance value. The fitted resistances are listed in table 7.1 and the $I - V$ curve is plotted with the fits in Fig. 7.3.

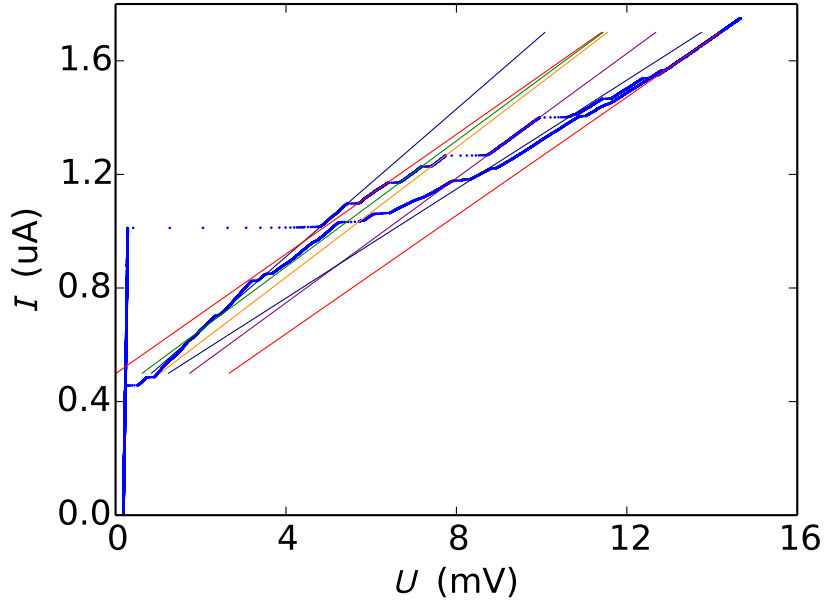


Figure 7.3: The steps in the up sweep were fitted with lines (Tab. 7.1). The resistance does not continuous increase with higher currents. All slopes can be found in the down sweep data again. For a better visibility not all fitted lines are plotted in this figure.

Table 7.1: Resistance for the different slopes in the up sweep at zero field. The difference in the resistance to the previous slope $\Delta R_{n,n-1}$ is listed.

slope number	R (k Ω)	$\Delta R_{n,n-1}$ (k Ω)
1	7.67	-
2	9.49	+1.80
3	9.01	-0.48
4	8.75	-0.26
5	9.11	+0.37
6	10.42	+1.31
7	10.84	+0.42
8	10.47	-0.36
9	10.28	-0.19
10	9.60	-0.68

While there is a tendency for the resistances to increase, the increase is not continuous with the step number.

The visible steps in the current-voltage measurement can be explained by the phase slip center model by Skocpol, Beasley, and Tinkham [19] (see Sec. 2.3). Due to weak superconducting spots in a wires, a location where the supercurrent is smallest, the current will reach its critical value there first. The order parameter fluctuates to zero and the phase of the order parameter slips by 2π , a voltage drops. Since the whole current is carried by normal conducting, the order parameter gets restored and the wire gets superconducting

again. The next step occurs, as the critical current for the next phase slip center is reached. Phase slip centers appear for temperatures near T_c . These temperatures are reached here locally due to the dissipation power in the order of nW and the low thermal conductivity of the superconducting wires and the SiO₂ substrate.

For currents $I \gtrsim 1.6 \mu\text{A}$ there are no steps in the curve and an ohmic behavior with a resistance $R_{ohm} \sim 9.6 \text{ k}\Omega$ can be found. Estimating the resistance for the nanowires in a parallel circuit results in

$$R_{array} = \frac{R_{wire}}{N} \approx \frac{40}{12} \text{ k}\Omega = 3.3 \text{ k}\Omega \quad (7.1)$$

Because of the high power dissipated into the system, some additional structures might get resistive as well. Taking into account all the structures up to the current distribution and estimating the number of squares we get (see Fig. 3.2): wires (~ 40 squares each), vertical leads inside the array ($\sim 2 \times 15$ squares) and vertical leads from array to the current distribution ($\sim 2 \times 13$ squares)

$$R_{est} \approx \left(\frac{(40 + 30)}{12} + \frac{26}{7} \right) \text{ k}\Omega = 9.54 \text{ k}\Omega \quad (7.2)$$

The measured resistance can be explained by resistive surrounding AlO_x structures due to the dissipated energy.

The magnetic field dependence was studied by measuring $I - V$ curves for multiple coil currents. The coil current was ramped up to 80 mA, creating a maximum magnetic field of 1.2 mT. For each coil current the measurement was performed analog to the one described above. The bias current was swept in low μA range.

The curves are very similar to the ones for zero field (Fig. 7.1). The sample is superconducting up to a critical current, before featuring a current plateau, a discontinuity in the voltage. This is followed by a step-structure with multiple plateaus and resistive slopes in between. The steps also appear in the down sweep. A hysteresis effect is observable, the down sweep curve lies below the curve of the up sweep. The supercurrent is observable in the down sweep at about 0.45 μA . While the curves do not change in their general appearance from the zero field measurement, they also stay quantitatively the same. The only exceptions are specific coil currents, where the critical current is suppressed by about 30 % to 0.7 μA .

These distinct magnetic fields show no periodicity or obvious pattern, but are reproducible for for multiple field sweeps and long waiting times in between. An $I - V$ curve featuring such a suppressed supercurrent is shown in Fig. 7.4, with an applied coil current of 17.5 mA. While the critical current is suppressed, the rest of the curve stays identical to the zero field measurement.

The periodic change in the critical current depending on the magnetic field, similar to a Fraunhofer diffraction pattern (Sec. 2.5) was not observed. The reason for this missing periodicity can be explained by the parameter $\beta_L = \frac{2\pi}{\Phi_0} LI$. This parameter is the ratio of the self-induced flux, generated by a circulating current in a loop compared to a flux quantum. It measures the number of flux quanta, that can be screened by the maximum critical current. The inductance is dominated by the kinetic part, $L_{kin} = 670 \text{ pH}/\square$ for an $R_\square = 1 \text{ k}\Omega$ AlO_x film.

$$\beta_L = \frac{2\pi}{\Phi_0} L \cdot I_c \approx \frac{2\pi}{\Phi_0} L_{kin} \cdot I_c \approx 22 \quad (7.3)$$

For such high screening, the junction does not feature a periodic magnetic field dependence. For smaller $\beta_L \ll 1$ a periodic pattern is expected.

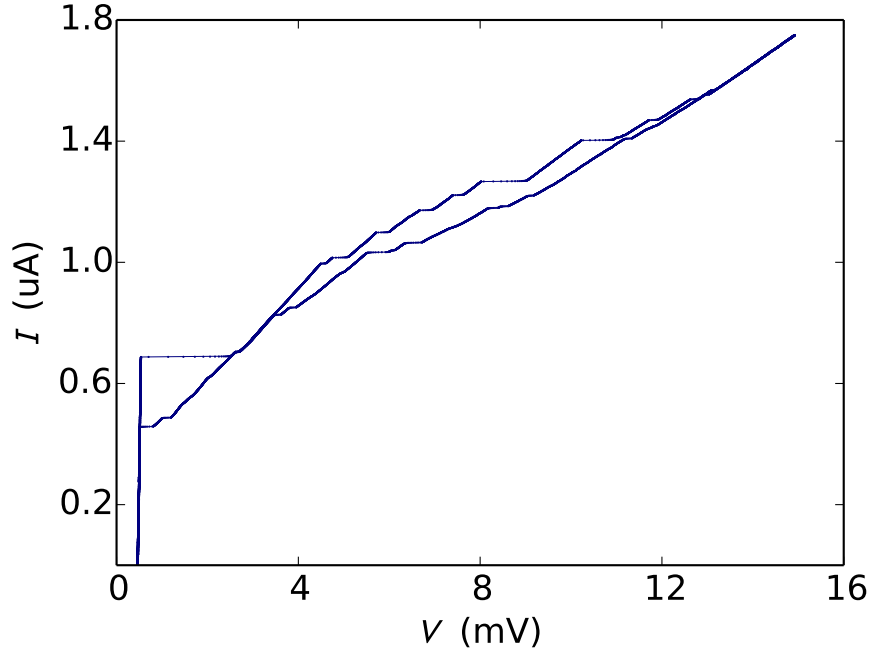


Figure 7.4: $I - V$ characteristics with $I_B = 17.5 \mu\text{A}$, $B \approx 525 \mu\text{T}$. The supercurrent is reduced by $\sim 30\%$ compared to the zero field curve, while the other plateau currents and the resistances of the slopes stay the same.

The $I - V$ characteristics is plotted in Fig. 7.5. The current was ramped up (see (1) in Fig. 7.5) to the ohmic range (2), but ramped down only to $0.5 \mu\text{A}$ (3). The system does not become superconducting. Starting at this point, multiple up and down sweeps were measured (4), each sweep starting at a different voltage level. The current is ramped up like the virgin sweep and down to its unique start. No magnetic field was applied.

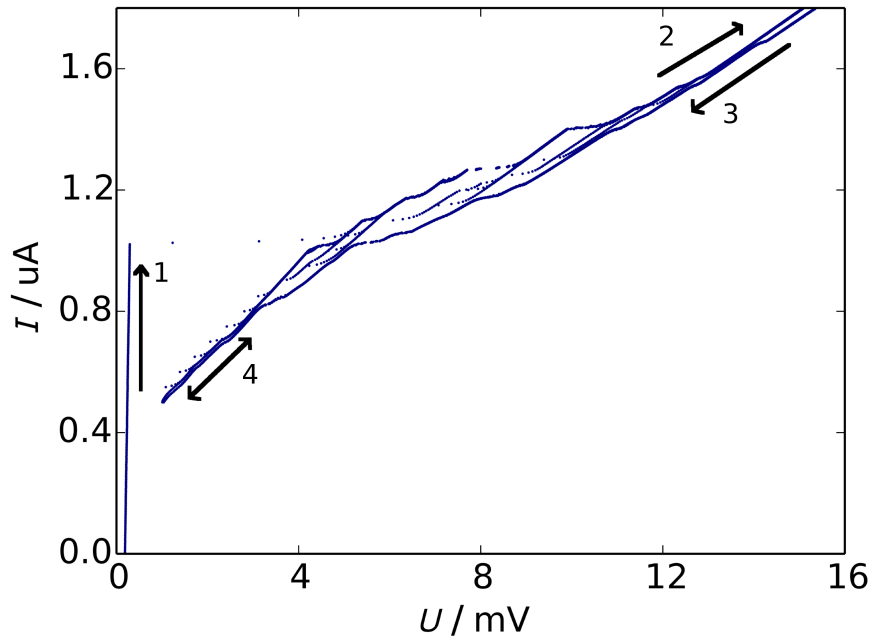


Figure 7.5: The different branches are measured by a first up sweep, going down almost into superconductivity again (1-3). From this point all further sweeps start, going up from increasing starting points (4).

In order to confirm the slopes appearing in the $I - V$ plots, a different sweep in the bias current was performed to enter these slopes at lower currents from below.

The virgin sweep is the same $I - V$ curve as described above. It shows the critical current, followed by the step-structure in up and down sweep. Each offset sweep starts in a resistive slope, which corresponds to a slope visible in the virgin curve. The system follows this slope until it crosses the virgin sweep. From there, it follows the original curve. Due to the increase of the starting current, there are sweeps starting in each slope of the system. Every down sweep shows the exact same re-trapping current behavior. The steps in the data are slightly rounded, an experimental artifact resulting from a fast measurement.

7.1.2 Voltage bias

Voltage bias was used to obtain more information about the sample at low voltages. Due to the discontinuity at a particular step in the current bias, no information is available about this range. For this measurement, the bias voltage was ramped in the low mV range, creating the same amount of μA response than observed in the current bias. No magnetic field was applied.

The data shows a linear current-voltage dependence up to nearly 0.6 mV. For higher voltages, the sample features a step-structure with discontinuities in the current, dropping to smaller values. Three of these steps occur before the sweep direction is reversed. The system shows a hysteresis effect, the discontinuities appear at smaller voltages in the down sweep, but then coincide with the up sweep data. The slope after the first discontinuity is not reached by the down sweep, the system shows directly a linear dependence from the beginning. This discontinuity in the down sweep is not as sharp as the others, but rounded before the increase in the current. The $I - V$ curve is plotted in Fig. 7.6. The data colored in red represents the up sweep, the blue colored data the down sweep. A shift in the sweep directions is visible even at very low voltages, this is due to charge reversal in the stray capacitance and the high resistance of the sample.

The resistive slopes were fitted to lines, with the reciprocal gradient representing the resistance. The resistances are listed in table 7.2.

Table 7.2: Resistance for the difference slopes measured in the voltage bias at zero field.

slope number	1	2	3	4
R ($\text{k}\Omega$)	0.72	5.24	4.90	5.63

The resistance for the first slope (725Ω) is given by the 2-wire load line from the room temperature electronics. As long as the sample is superconducting, no voltage drops over the chip. The resistance of the wiring is therefore orders of magnitudes larger. As soon as the sample gets resistive, the resistance is much higher than the load line and it can be neglected. The measured resistance coincides with comparable room temperature measurements prior to starting the measurements. The scheme is depicted in Fig. 7.7.

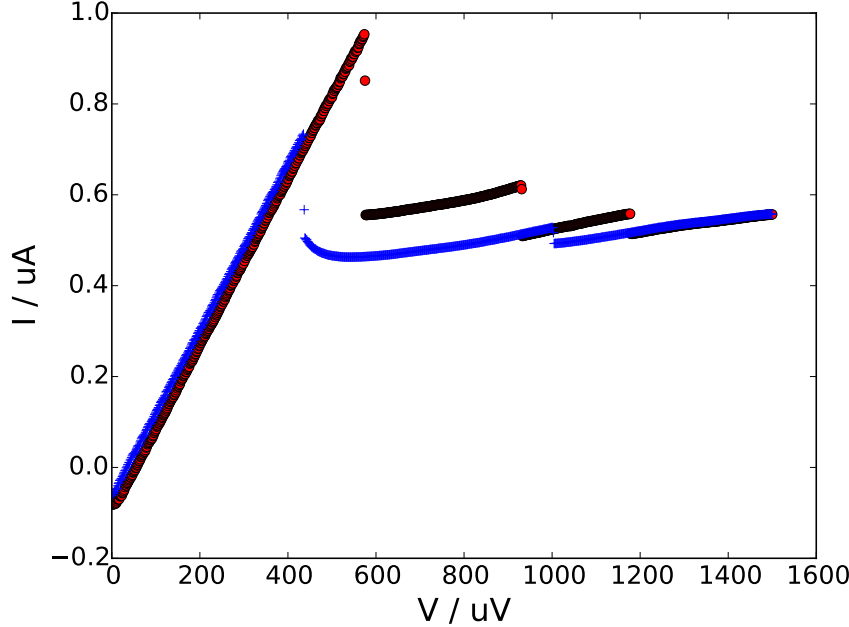


Figure 7.6: $I - V$ curve for zero field with a voltage bias in low mV range. The array shows results similar to the current bias with a step structure explained by phase slip centers. The first resistive slope comes from the load line while the sample is still superconductive (Fig. 7.7).

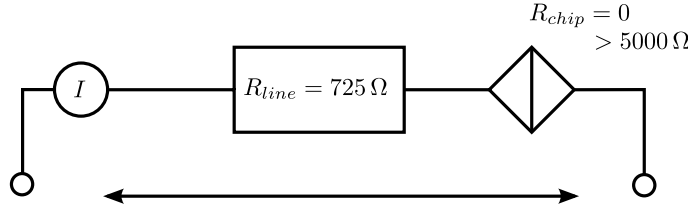


Figure 7.7: While the sample is superconducting a voltage drops over the measurement wires and lead to a resistance. As soon as the sample shows a voltage drop, the resistance coming from the wires is an order of magnitude higher than the load line resistance.

The steps match again the phase slip center models due to heating, with resistance slightly lower, but of the same order than the ones measured current biased. The heat explains the hysteresis effect, the warmed phase slip center has a lower critical current and needs to cool down in order to vanish.

The magnetic field dependence was studied for coil currents up to ± 50 mA (≈ 1.5 mT). The sample follows the same magnetic dependence as described above. The curves show in the same behavior in a magnetic field as for zero field, in quality as in quantity. Only at distinct coil currents the behavior differs. The sample gets resistive at lower voltages and phase slip center steps occur at lower voltage values, matching the result from the current biased measurements due to $\beta_L \sim 22$. The resistance in the slopes does not change. Such data is shown in figure 7.8.

These different curves occur at reproducible magnetic field values, but without any periodicity or obvious pattern. The color plot in figure 7.9 shows the measured data color coded. The applied voltage is shown on the y-axis, while the ramped magnetic field is shown on the x-axis. The measured current is color coded, increasing from blue to red. The datasets

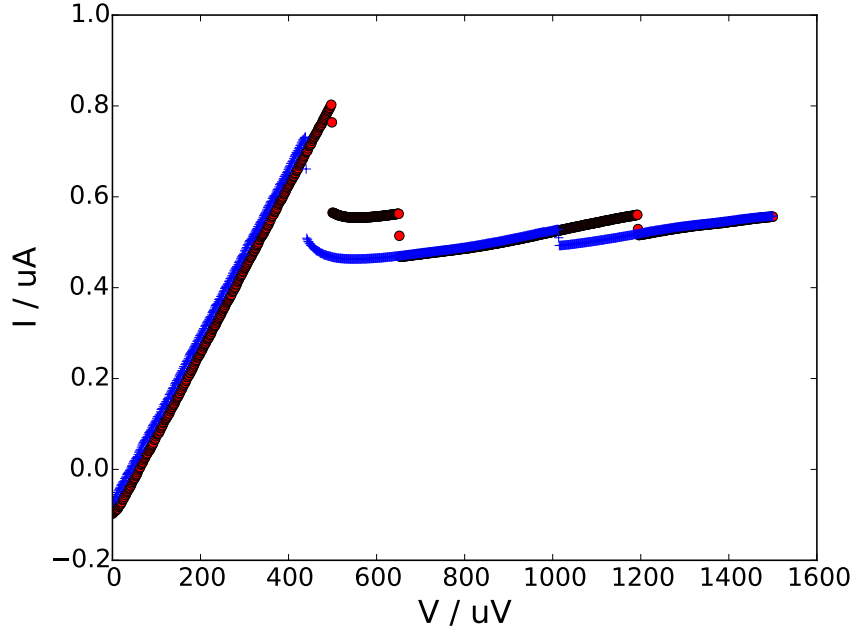


Figure 7.8: $I - V$ curve at a coil current $I_B = 5.33 \text{ mA}$ ($\sim 160 \mu\text{T}$). The steps into the next slope occur at an earlier voltage value as at zero field.

with different behavior can be seen by sharp vertical lines showing a significant difference in color, for example at $I_B \sim 29 \text{ mA}$.

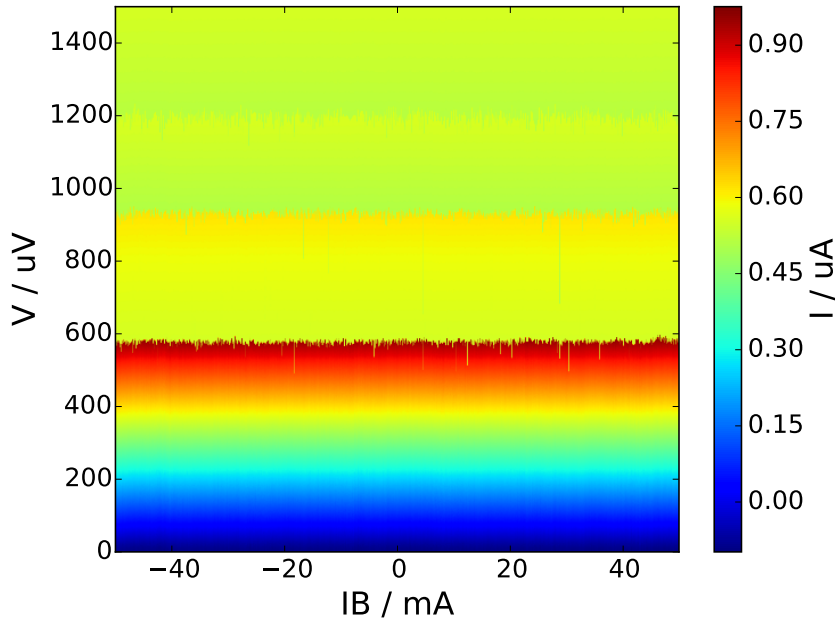


Figure 7.9: Color plot of V versus coil current I_B with colored I . The sharp lines in the plot indicate the reproducible field values, for which the behavior of the array differs. The values do not show any periodicity.

7.2 Parallel array with 0.75 μm -nanowires

7.2.1 Current bias

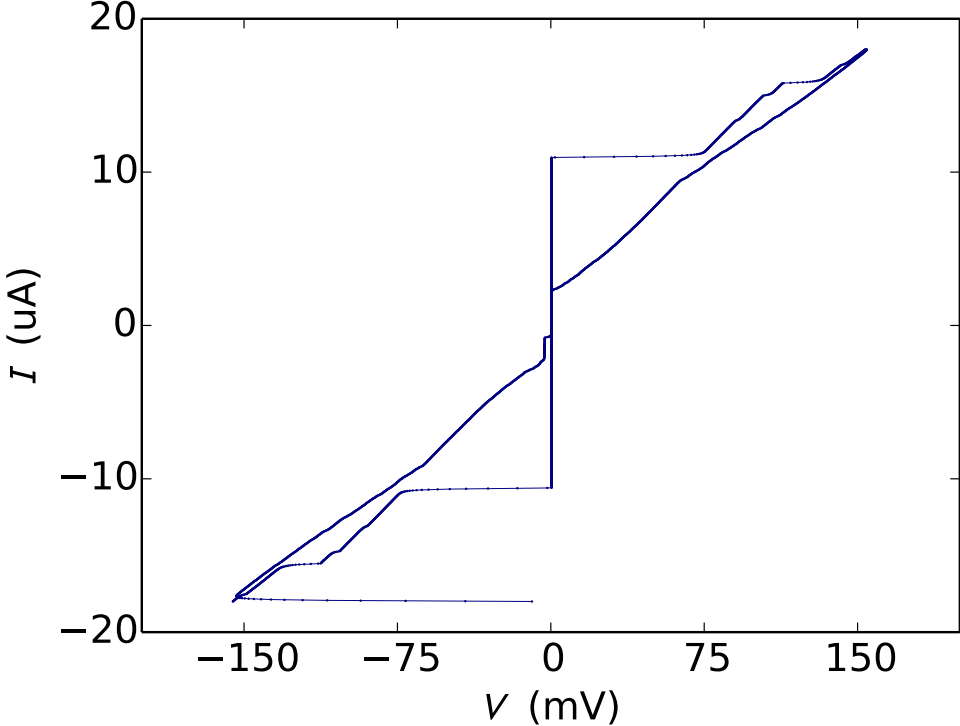


Figure 7.10: $I - V$ curve, current biased for zero field. The current is ramped in $\pm 20 \mu\text{A}$ range. A superconducting behavior is followed by a step structure and an ohmic behavior. The down sweep shows bumps instead of steps.

This sample was measured by ramping the bias current in the order of $\pm 20 \mu\text{A}$ in both directions, with no magnetic field applied. The response was in the order of $\pm 100 \text{ mV}$. The plots are very similar to the ones for the array described above. The sample shows superconductivity up to $I_c \sim \pm 10 \mu\text{A}$, then features a discontinuity in the voltage followed by a step-like structure: A slope with a linear increase in voltage is followed by a discontinuity, forming a current plateau. The down sweep features bumps instead of real steps. The plot shows a hysteresis in the system, with the curve of the down sweep located closer to the x-axis. For currents below I_c the system does not get superconducting immediately, for I below 30 % of the critical current no voltage drops occurs. The resulting $I - V$ curve is plotted in Fig. 7.10. The measurement speed rounds the steps and is also responsible for the bumps instead of real steps in the down sweep. The plot features two measurement artifacts. One being the line of constant current at the very bottom, indicating the beginning of the measurement, the other one is a step near $I \sim 0$, which was not seen in other measurements.

The critical current $I_c \approx \pm 10 \mu\text{A}$ is a factor of 10 higher than in the array with 1 μA wire length. There is a slight difference between the positive and negative critical current due to a current offset, with the positive critical current being slightly larger in absolute value.

The current values of the plateaus in both up sweep directions are plotted against the corresponding number of plateau in Fig. 7.2(a), showing a linear dependence for both groups of four plateaus. The plateaus were numbered by starting at 1 at the lower current, going to 10 for the highest. The same can be found for the voltage (Figs. 7.2(b)) For the voltage dependence, the last voltage value of each plateau was plotted against the

corresponding number Tor the power was calculated using the corresponding current and voltage values. The power dependence 7.2(c) shows linear dependence for each group of plateaus. The power values for the groups coincide 7.2(d)).

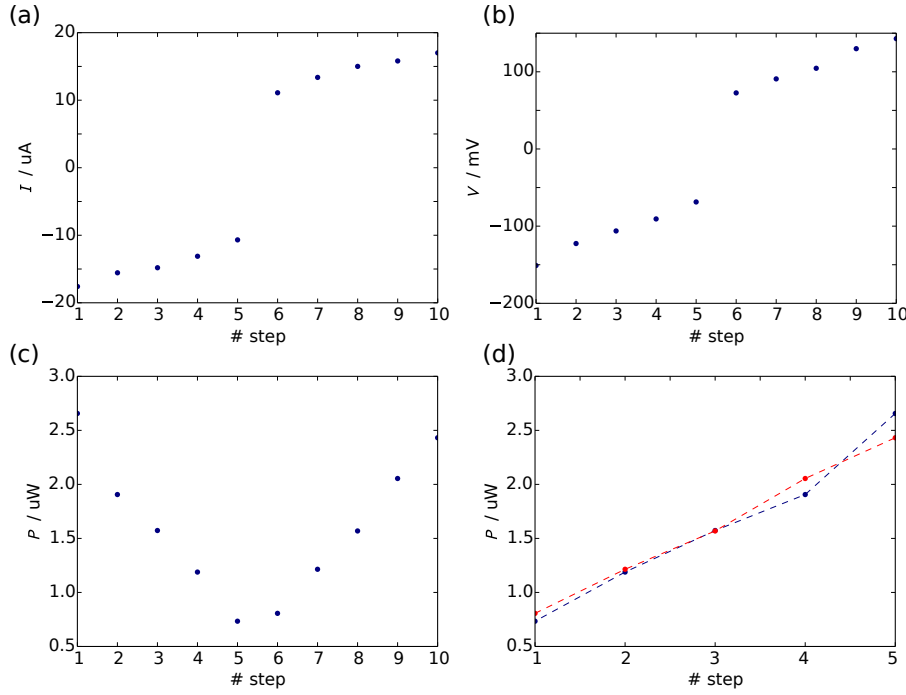


Figure 7.11: (a) Current on plateau versus number of plateau. (b) Last voltage value of plateau versus number of plateau. (c) Dissipated power $P = U \cdot I$, on plateau versus number of plateau. (d) The power values coincide for both groups of plateaus. The plateaus at negative current values are colored in blue, the positive plateaus are colored in red.

The slopes connecting the different plateaus feature a linear current-voltage dependence and were fitted into lines using the data from the up sweep. The gradient of each fit represents a constant resistance value. The fitted resistances are listed in table 7.1 and a plot featuring the fitted data is depicted in Fig. 7.12. The plotted $I - V$ is zoomed in and only the up sweep for negative current values was plotted due to better visibility.

Table 7.3: Resistance for the different slopes in the up sweep at zero field. The difference in the resistance to the previous slope in the current range ΔR_{ij} is listed.

slope number	R ($\text{k}\Omega$)	ΔR_{ij} $\text{k}\Omega$
1	8.64	+0.20
2	8.44	+1.21
3	7.23	+0.25
4	6.98	+0.15
5	6.83	-
6	6.72	-
7	6.84	+0.09
8	7.17	+0.73
9	8.51	+1.34
10	8.70	+0.19

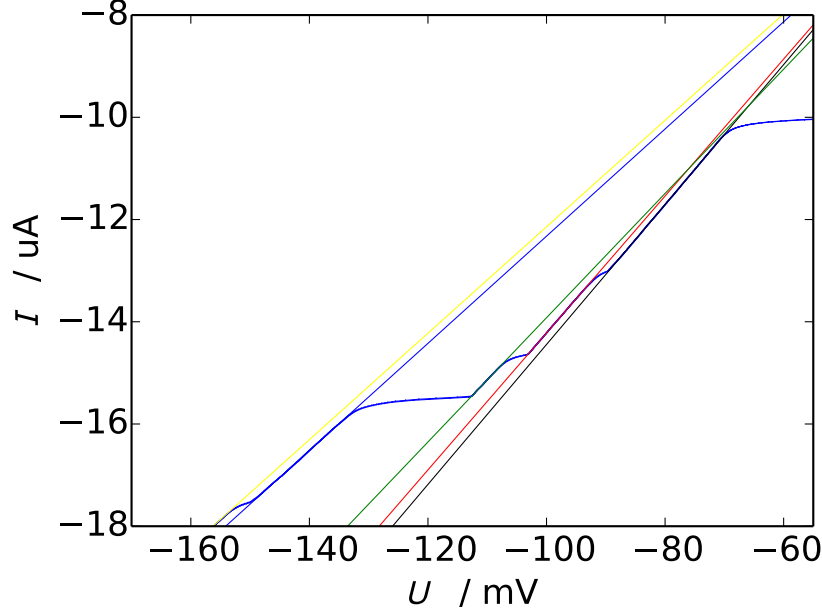


Figure 7.12: In up sweep data for negative current values, the slopes were fitted with lines. Note the zoomed scale.

We see again a step structure corresponding to the phase slip center model. The dissipation power in the milli-Watt range together with the low thermal conduction of SiO_2 heats the chip and the critical current of phase slip centers is reached.

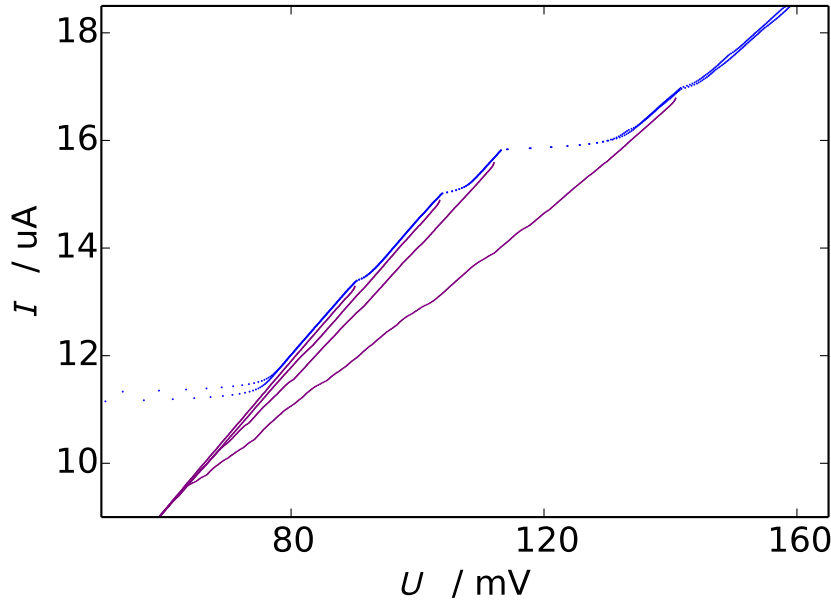


Figure 7.13: The different branches are entered form above by changing the value for the current to change directions. All slopes connect at one point in the re-trapping branch. Note the zoomed scale.

For currents $I \gtrsim \pm 17 \mu\text{A}$ the gets ohmic with a resistance $R_{ohm,+} \sim 8.64 \text{ k}\Omega$ and $R_{ohm,-} \sim 8.70 \text{ k}\Omega$. Performing a similar estimation as in Eq. (7.2), by taking into account that all

structures up to the current distribution get normal conductive due to dissipation, we find: wires (~ 30 squares each) + vertical leads inside the array ($\sim 2 \times 16$ squares) and the vertical leads from array to current distribution ($\sim 2 \times 13$ squares)

$$R_{est} \approx \left(\frac{(30+32)}{12} + \frac{26}{7} \right) \text{k}\Omega = 8.88 \text{k}\Omega \quad (7.4)$$

The influence of the magnetic field on the critical current was studied for coil currents up to $20 \mu\text{A}$ ($\sim 600 \mu\text{T}$). At this sample the critical current shows no magnetic field dependence. This can be explained by the factor β_L again. For this critical current we find

$$\beta_L = \frac{2\pi}{\Phi_0} L_{kin} I_c \approx 220 \gg 1 \quad (7.5)$$

A periodic magnetic field dependence is expected for values of $\beta_L \lesssim 1$.

In order to confirm the slopes in the $I - V$ plot, a different sweep was applied to enter these slopes from above. The current was ramped up each time to a different turning point and down again to zero. That way the system enters different re-trapping branches and multiple slopes get visible. The up sweep follows every time the behavior described above, after losing superconductivity the data shows a step structure with discontinuities in the voltage. In all down sweeps no steps, but bumps are visible. At some point all down sweeps connect to a single branch. The data is plotted in Fig. 7.13. For visibility reason the data is zoomed in and only the last two up sweeps are depicted. The up sweep data is colored in blue, while the down sweeps are colored in violet. The steps are rounded due to the measurement speed.

8 Conclusion

In this theses, the ground work for transport measurements on arrays of superconducting AlO_x nanowires been laid by designing, fabricating and performing the first four-point probes measurements of such samples at milli-Kelvin temperatures.

Multiple arrays aiming to lumped elements and flux localization were designed and fabricated, allowing measurement of multiple parameters like the wire length and wire number in a DC current or DC voltage biased setup.

The sample preparation has been optimized for transport measurement, enabling galvanic contact between the coarse structures defined by optical lithography and the nanowire arrays defined by electron-beam lithography. The fabrication of the nanowires has been optimized to reach a reproducible wire width of smaller than 30 nm, while leaving the film unharmed by a Cl^- -based reactive ion etch process.

Four-point probes measurement at milli-Kelvin temperatures were performed to analyze the $I - V$ characteristics in current and voltage bias depending on an applied magnetic field. The studied arrays featured 12 parallel nanowires with a nominal width of 25 nm and wire lengths of 0.75 μm and 1 μm . The samples showed both superconducting behavior, with a length dependent critical current in the μA range. A tendency was found to get smaller critical currents by increasing the wire length.

In $I - V$ measurements a step structure was found in the characteristics above the critical current with voltage drops in the mV range. This can be explained by the phase slip center model by Skocpol, Beasley, and Tinkham [19], creating a voltage drop due to phase slips in local weak spots in the wires. The influence of the magnetic field on the sample are weak, due to the high critical current and the high kinetic inductance of the used material. Influences, suppressing the critical current to about 30 % of its original value were found at certain magnetic field values. The values show no obvious pattern or periodic structure, but are reproducible in many measurements over a long period of time.

In order to observe quantum phase slip effects, the critical current has to be reduced. This can be done most probably by further increase of the wire length in the array.

References

- [1] W. A. Little: *Decay of Persistent Currents in Small Superconductors*. Phys. Rev. **156**(2):396 (1967)
- [2] J. S. Langer and V. Ambegaokar: *Intrinsic Resistive Transition in Narrow Superconducting Channels*. Phys. Rev. **164**(2):498 (1967)
- [3] D. E. McCumber and B. I. Halperin: *Time Scale of Intrinsic Resistive Fluctuations in Thin Superconducting Wires*. Phys. Rev. B **1**(3):1054 (1970)
- [4] N. Giordano: *Evidence for macroscopic quantum tunneling in one-dimensional superconductors*. Phys. Rev. Lett. **61**(18):2137 (1988)
- [5] J. E. Mooij and Y. V. Nazarov: *Superconducting nanowires as quantum phase-slip junctions*. Nature Phys. **2**(3):169 (2006)
- [6] O. V. Astafiev, L. B. Ioffe, S. Kafanov, Y. A. Pashkin, K. Y. Arutyunov, D. Shahar, O. Cohen, and J. S. Tsai: *Coherent quantum phase slip*. Nature **484**(7394):355 (2012)
- [7] Kamerlingh Onnes, H.: *Further experiments with Liquid Helium G. On the electrical resistance of Pure Metals etc. VI. On the Sudden Change in the Rate at which the Resistance of Mercury Disappears*. P. K. Ned. Akad. B Phys. **14**(2):818 (1911)
- [8] W. Meissner and R. Ochsenfeld: *Ein neuer Effekt bei Eintritt der Supraleitfähigkeit*. Naturwissenschaften **21**(44):787 (1933)
- [9] F. London and H. London: *The Electromagnetic Equations of the Supraconductor*. Proc. R. Soc. London, Ser. A **149**(866):71 (1935)
- [10] V. L. Ginzburg and L. D. Landau: *On the theory of superconductivity*. Zh. Eksp. Teor. Fiz. **20**:1064 (1959). English translation in: L. D. Landau, Collected papers (Oxford: Pergamon Press, 1965) p. 546
- [11] F. Altomare and A. M. Chang: *One-Dimensional superconductivity in nanowires*. Wiley-VCH Verlag GmbH & Co. KGaA Weinheim (2013)
- [12] L. N. Cooper: *Bound Electron Pairs in a Degenerate Fermi Gas*. Phys. Rev. **104**(4):1189 (1956)
- [13] J. Bardeen, L. N. Cooper, and J. R. Schrieffer: *Theory of Superconductivity*. Phys. Rev. **108**(5):1175 (1957)
- [14] B. Josephson: *Possible new effects in superconductive tunnelling*. Phys. Lett. **1**(7):251 (1962)
- [15] R. P. Feynman: *The Feynman Lectures on Physics*. Volume 3. Addison-Wesley 2 edition (2005)
- [16] S. Shapiro: *Josephson Currents in Superconducting Tunneling: The Effect of Microwaves and Other Observations*. Phys. Rev. Lett. **11**(2):80 (1963)

- [17] N. D. Mermin and H. Wagner: *Absence of Ferromagnetism or Antiferromagnetism in One- or Two-Dimensional Isotropic Heisenberg Models.* Phys. Rev. Lett. **17**(22):1133 (1966)
- [18] A. J. Kerman: *Flux-charge duality and topological quantum phase fluctuations in quasi-one-dimensional superconductors.* New J. Phys. **15**(10):105017 (2013)
- [19] W. J. Skocpol, M. R. Beasley, and M. Tinkham: *Phase-slip centers and nonequilibrium processes in superconducting tin microbridges.* J. Low Temp. Phys. **16**(1-2):145 (1974)
- [20] J. D. Meyer and G. v. Minnigerode: *Instabilities in the transition curve of current-carrying one-dimensional superconductors.* Phys. Lett. A **38**(7):529 (1972)
- [21] J. D. Meyer: *Spannungsstufen in den U(T)-Übergangskurven und U(I)-Kennlinien stromtragender Zinn-Whisker.* Appl. Phys. A **2**(6):303 (1973)
- [22] V. V. Schmidt: *The Physics of Superconductors: Introduction to Fundamentals and Applications.* P. Müller and A. V. Ustinov (editors). Springer (1997)
- [23] J. E. Lukens, R. J. Warburton, and W. W. Webb: *Onset of Quantized Thermal Fluctuations in "One-Dimensional" Superconductors.* Phys. Rev. Lett. **25**(17):1180 (1970)
- [24] R. S. Newbower, M. R. Beasley, and M. Tinkham: *Fluctuation Effects on the Superconducting Transition of Tin Whisker Crystals.* Phys. Rev. B **5**(3):864 (1972)
- [25] A. Bezryadin, C. N. Lau, and M. Tinkham: *Quantum suppression of superconductivity in ultrathin nanowires.* Nature **404**(6781):971 (2000)
- [26] C. N. Lau, N. Markovic, M. Bockrath, A. Bezryadin, and M. Tinkham: *Quantum Phase Slips in Superconducting Nanowires.* Phys. Rev. Lett. **87**(21):217003 (2001)
- [27] F. Altomare, A. M. Chang, M. R. Melloch, Y. Hong, and W. T. Charles: *Evidence for macroscopic quantum tunneling of phase slips in long one-dimensional superconducting Al wires.* Phys. Rev. Lett. **97**(1):017001 (2006)
- [28] M. Zgirski, K.-P. Riikonen, V. Touboltsev, and K. Y. Arutyunov: *Quantum fluctuations in ultranarrow superconducting aluminum nanowires.* Phys. Rev. B **77**(5):054508 (2008)
- [29] J. S. Lehtinen, T. Sajavaara, K. Y. Arutyunov, M. Y. Presnjakov, and A. L. Vasiliev: *Evidence of quantum phase slip effect in titanium nanowires.* Phys. Rev. B **85**(9):094508 (2012)
- [30] N. Giordano: *Superconductivity and dissipation in small-diameter Pb-In wires.* Phys. Rev. B **43**(1):160 (1991)
- [31] A. Bezryadin: *Superconductivity in Nanowires.* Wiley-VCH Verlag GmbH & Co. KGaA Weinheim (2012)
- [32] A. D. Zaikin, D. S. Golubev, A. van Otterlo, and G. T. Zimányi: *Quantum phase slips and transport in ultrathin superconducting wires.* Phys. Rev. Lett. **78**(8):1552 (1997)
- [33] M. Tinkham: *Introduction to Superconductivity.* Dover books on physics and chemistry. Dover Publications (2004)
- [34] D. S. Golubev and A. D. Zaikin: *Quantum tunneling of the order parameter in superconducting nanowires.* Phys. Rev. B **64**(1):014504 (2001)
- [35] V. Ambegaokar and B. I. Halperin: *Voltage Due to Thermal Noise in the DC Josephson Effect.* Phys. Rev. Lett. **22**(25):1364 (1969)

- [36] T. A. Fulton and L. N. Dunkleberger: *Lifetime of the zero-voltage state in Josephson tunnel junctions*. Phys. Rev. B **9**(11):4760 (1974)
- [37] Nakamura Y., Pashkin Yu. A., and Tsai J. S.: *Coherent control of macroscopic quantum states in a single-Cooper-pair box*. Nature **398**(6730):786 (1999)
- [38] J. E. Mooij and C. J. P. M. Harmans: *Phase-slip flux qubits*. New J. Phys. **7**(1):219 (2005)
- [39] A. M. Hriscu and Y. V. Nazarov: *Model of a proposed superconducting phase slip oscillator: a method for obtaining few-photon nonlinearities*. Phys. Rev. Lett. **106**(7):077004 (2011)
- [40] A. M. Hriscu and Y. V. Nazarov: *Coulomb blockade due to quantum phase slips illustrated with devices*. Phys. Rev. B **83**(17):174511 (2011)
- [41] J. Peltonen, O. Astafiev, Y. Korneeva, B. Voronov, A. Korneev, I. Charaev, A. Semenov, G. Golt'sman, L. Ioffe, T. Klapwijk, and J. Tsai: *Coherent flux tunneling through NbN nanowires*. Phys. Rev. B **88**(22):220506 (2013)
- [42] K. Y. Arutyunov, T. T. Hongisto, J. S. Lehtinen, L. I. Leino, and A. L. Vasiliev: *Quantum phase slip phenomenon in ultra-narrow superconducting nanorings*. Sci. Rep. **2**(293) (2012)
- [43] J. S. Lehtinen, K. Zakharov, and K. Y. Arutyunov: *Coulomb blockade and Bloch oscillations in superconducting Ti nanowires*. Phys. Rev. Lett. **109**(18):187001 (2012)
- [44] T. T. Hongisto and A. B. Zorin: *Single-charge transistor based on the charge-phase duality of a superconducting nanowire circuit*. Phys. Rev. Lett. **108**(9):097001 (2012)
- [45] P. Giacomo: *News from the BIPM*. Metrologia **25**(2):113 (1988)
- [46] J. E. Mooij, G. Schön, A. Shnirman, T. Fuse, C. J. P. M. Harmans, H. Rotzinger, and A. H. Verbruggen: *Superconductor-insulator transition in nanowires and nanowire arrays* arXiv:1410.6140v1 [cond-mat.supr-cond] (2014)
- [47] P. Fehlner: *Developing nano-scale Josephson tunnel junctions for qubits*. Master's Thesis, Karlsruhe Institute of Technology (2014)
- [48] J. Rowell: *Magnetic Field Dependence of the Josephson Tunnel Current*. Phys. Rev. Lett. **11**(5):200 (1963)
- [49] F. Bloch: *Über die Quantenmechanik der Elektronen in Kristallgittern*. Z. Phys. **52**(7-8):555 (1928)
- [50] C. Zener: *A Theory of the Electrical Breakdown of Solid Dielectrics*. Proc. R. Soc. London, Ser. A **145**(885):523 (1934)
- [51] D. V. Averin, A. B. Zorin, and K. K. Likharev: *Bloch oscillations in small Josephson junctions*. Zh. Eksp. Teor. Fiz. **88**:692 (1985). English translation in: Soviet Physics JETP **61**, 407 (1985)
- [52] K. K. Likharev and A. B. Zorin: *Theory of the Bloch-wave oscillations in small Josephson junctions*. J. Low Temp. Phys. **59**(3-4):347 (1985)
- [53] L. S. Kuzmin and D. B. Haviland: *Observation of the Bloch oscillations in an ultra-small Josephson junction*. Phys. Rev. Lett. **67**(20):2890 (1991)
- [54] M. Sahu, M.-H. Bae, A. Rogachev, D. Pekker, T.-C. Wei, N. Shah, P. N. Golbart, and A. Bezryadin: *Individual topological tunnelling events of a quantum field probed through their macroscopic consequences*. Nature Phys. **5**(7):503 (2009)

- [55] T. Aref, A. Levchenko, V. Vakaryuk, and A. Bezryadin: *Quantitative analysis of quantum phase slips in superconducting Mo₇₆Ge₂₄ nanowires revealed by switching-current statistics.* Phys. Rev. B **86**(2):024507 (2012)
- [56] J. S. Lehtinen and K. Y. Arutyunov: *The quantum phase slip phenomenon in superconducting nanowires with a low-Ohmic environment.* Supercond. Sci. Technol. **25**(12):124007 (2012)
- [57] C. H. Webster, J. C. Fenton, T. T. Hongisto, S. P. Giblin, A. B. Zorin, and P. A. Warburton: *NbSi nanowire quantum phase-slip circuits: DC supercurrent blockade, microwave measurements and thermal analysis.* Phys. Rev. B **87**(14):144510 (2013)
- [58] G. Deutscher, H. Fenichel, M. Gershenson, E. Grünbaum, and Z. Ovadyahu: *Transition to zero dimensionality in granular aluminum superconducting films.* J. Low Temp. Phys. **10**(1-2):231 (1973)
- [59] H. Rotzinger, S. T. Skacel, M. Pfirrmann, J. N. Voss, J. Münzberg, S. Probst, P. Busshev, M. P. Weides, A. V. Ustinov, and J. E. Mooij: *Sputter deposited aluminium-oxide for superconducting high kinetic inductance circuits* arXiv:1408.4347v2 [cond-mat.supr-cond] (2014)
- [60] J. N. Voss: *Fabrication and characterization of metallic aluminium oxide films.* Bachelor's Thesis, Karlsruhe Institute of Technology (2014)
- [61] J. Münzberg: *Characterization of annealed metallic aluminum oxide films.* Bachelor's Thesis, Karlsruhe Institute of Technology (2014)
- [62] C. Enss and S. Hunklinger: *Tieftemperaturphysik.* Springer Berlin (2000)
- [63] A. M. Dieter. Master's Thesis, Karlsruhe Institute of Technology (2015)
- [64] F. C. M. J. M. van Delft: *Delay-time and aging effects on contrast and sensitivity of hydrogen silsesquioxane.* J. Vac. Sci. Technol., B **20**(6):2932 (2002)

Appendix

A Fabrication recipe

In this section, the fabrication recipe for our investigated chips is listed. The recipe(s) are reproducible but as always, there is still some space for improvement left. Figure A.1 shows a schematic diagram containing all the fabrication processes.

Since the fabrication of chip investigated here, some recipe improvements have been made. These are marked in the tables, as well as suggestions for further parameters.

A.1 AlO_x deposition

Before deposition, an argon plasma is used to clean the substrate in-situ from water and organic residue. The sheet resistance of the AlO_x films is controlled using the Ar partial pressure. The Ar/O₂ partial pressure is kept constant. The process involves two pre-sputter processes for conditioning. The first one with a pure argon plasma, the second one with oxygen present in the main chamber. The sputtered films are about 20 nm thick. Some test runs may be necessary to get the wanted resistance.

Table A.1: Argon cleaning in load lock (LL)

Power (W)	LL pressure (mbar)	Ar flow (sccm)	Time (s)
20	$1.44 \cdot 10^{-1}$	10.5	120

Table A.2: Pre-sputter parameters

Pre-sputter process	Power (W)	MC pressure (Baratron) (μbar)	Ar flow (sccm)	Ar/O ₂ flow (sccm)	Time (s)
1	100	7.58	31.0	-	300
2	100	7.58	28.0	2.4	60

Table A.3: AlO_x deposition parameters

Power (W)	MC pressure (Baratron) (μbar)	Ar flow (sccm)	Ar/O ₂ flow (sccm)	Time (s)	Resistance on bank ¹ (kΩ)
100	7.58	28.0	2.4	210	2.9

¹We use a two-square rectangular SiO₂ chip for fast feedback of the sheet resistance. Comparative measurement however suggest a division by a factor of 3 to get the real sheet resistance.

A.2 Niobium deposition

A niobium layer is used to protect the aluminium-oxide from getting etched by the resist developer. This process is not implemented in the *PLASSYS MEB 550S* shadow evaporator and has to be done using manual control. A quartz crystal monitors rate and film thickness.

The niobium layer does change the resistance of the system only in the order of 10Ω , which is negligible regarding the resistance of our films in the range of $1\text{k}\Omega/\square$.

Table A.4: Nb deposition parameters

Deposition rate (nm/s)	Thickness (nm)	Base pressure (mbar)
0.004	5	$4.4 \cdot 10^{-8}$

A.3 Electron-beam lithography

Dow Corning XR-1541-002, a 2 % hydrogen silsesquioxane (HSQ) dilution in MIBK is used as a negative tone e-beam resist. Stored in a refrigerator, it has to stand 20 min at room temperature to acclimatize before spinning. The chip is cleaned for 5 min in isopropyl alcohol and rinsed in double-distilled water. After spinning, the chip rests for 5 min before being put on the hot plate. After the writing, the chip is developed using *Clariant AZ 726 MIF* developer.

The table below lists two different spin recipes, the second one is the one to use. The HSQ is here about 80 nm thick.

Table A.5: HSQ spinning parameters

Ramp speed, Ramp time (rpm), (s)	Full speed, Spin time (rpm), (s)	Acceleration (rmp/s)	Hot plate temperature, Hot plate time (°C), (s)
300, 10	4000, 60	7500	150, 120
new: 300, 10	4500, 60	7500	150, 120

The HSQ is spun onto the chip just before installing it into the e-beam lithography system.

Table A.6: HSQ exposure parameters

Base dose (area) ($\mu\text{C}/\text{cm}^2$)	Wire dose factor	Current (fine) (pA)	Current (coarse) (pA)	Lithography time (h)
600	9.17	1000	100	~ 3
suggested: 350	15.71	1000	100	~ 3

The point spread function describes a three-dimensional diffraction pattern of electrons emitted from an infinitely small point source. The function was simulated with a Monte Carlo method using *NEA-1525 PENELOPE2011*. The simulated substrate stack consisted of 3.5 μm Si, 400 nm SiO_2 , 20 nm Al_2O_3 , 5 nm Nb and 60 nm HSQ. Since the simulation database has no information about the AlO_x , we used aluminium(III) oxide instead. Later measurements indicated the HSQ to be 80 nm instead of 60 nm thick.

$$PSF = \frac{1}{\pi(1+\eta)} \left[\frac{1}{\alpha^2} e^{-\frac{r^2}{\alpha^2}} + \frac{\eta}{\beta^2} e^{-\frac{r^2}{\beta^2}} \right] \quad (8.1)$$

Table A.7: PSF parameters

α (μm)	β (μm)	η	z (nm)
0.002205	8.958633	0.798738	25

It is crucial to develop the structures immediately after removing it from the lithography system. The written HSQ structures would “age” and become wider with time [64].

Table A.8: HSQ development parameters

Developer	Time (s)	Rinse
AZ 726 MIF	60	H_2O

A.4 Optical lithography

Clariant AZ-5214E is used as a positive tone optical resist. It is about 1 μm thick. After spinning, the chip rests for 30 s before being put on the hot plate.

The chip is exposed using a *SUSS MicroTech Karl Suss MA6* mask aligner.

Table A.9: *AZ-5214E* spinning parameters

Ramp speed, Ramp time (rpm), (s)	Full speed, Spin time (rpm), (s)	Acceleration (rmp/s)	Hot plate temperature, Hot plate time ($^{\circ}\text{C}$), (s)
500, 5	6000, 60	7500	110, 50

Table A.10: *AZ-5214E* exposure parameters using *Karl Suss MA 6* mask aligner

Mask	Mode	Power (W)	Intensity (mW/cm^2)	Time (s)
Chrome/soda	Hard	275	5	7

Table A.11: *AZ-5214E* development parameters

Developer	Time (s)	Rinse
AZ 726 MIF	50	H_2O

A.5 ICP etching

Oxford Plasmalab100 ICP is used to transfer the resist pattern into the AlO_x . For good results the etching chamber is conditioned for 15 min before the main etch process. In addition, a 4“- SiO_2 wafer is used as a carrier for this process only.

Table A.12: ICP etch recipe for AlO_x structuring

Gas flow (sccm)	MC pressure (mTorr)	Power RIE (W)	Power ICP (W)	DC-Bias (V)
Cl ₂ : 12	10.0	100	200	420 – 500
Ar : 2				

Table A.13: ICP etch procedure

Process	Time (min)
Conditioning	15
Main etch	1.5
O ₂ -clean	20

To determine the etching rates for the different materials, we covered them with a thin microscope cover glass to create an edge. We etched for 2 min and determined the step height. Since the exposed HSQ resist is basically SiO₂ we used a piece of passivated wafer.

Table A.14: Etching rates for Cl/Ar 6:1 ICP/RIE plasma

Material	Etch rate (nm/min)
Si	250
SiO ₂	31
AlO _x	21

A.6 Resist strip

Only the optical resist can be stripped. The HSQ and the Nb layer remain on the etched structures. This is not a perfect solution and leaves space for some improvement.

Table A.15: Stripping the optical resist

Stripper	Ultrasonic cleaning level (arb. unit)	Time	Rinse
NEP ²	1	5 min at rest 15 s in cleaning bath 2 cycles	isopropyl alcohol H ₂ O

²N-ethyl-2-pyrrolidone

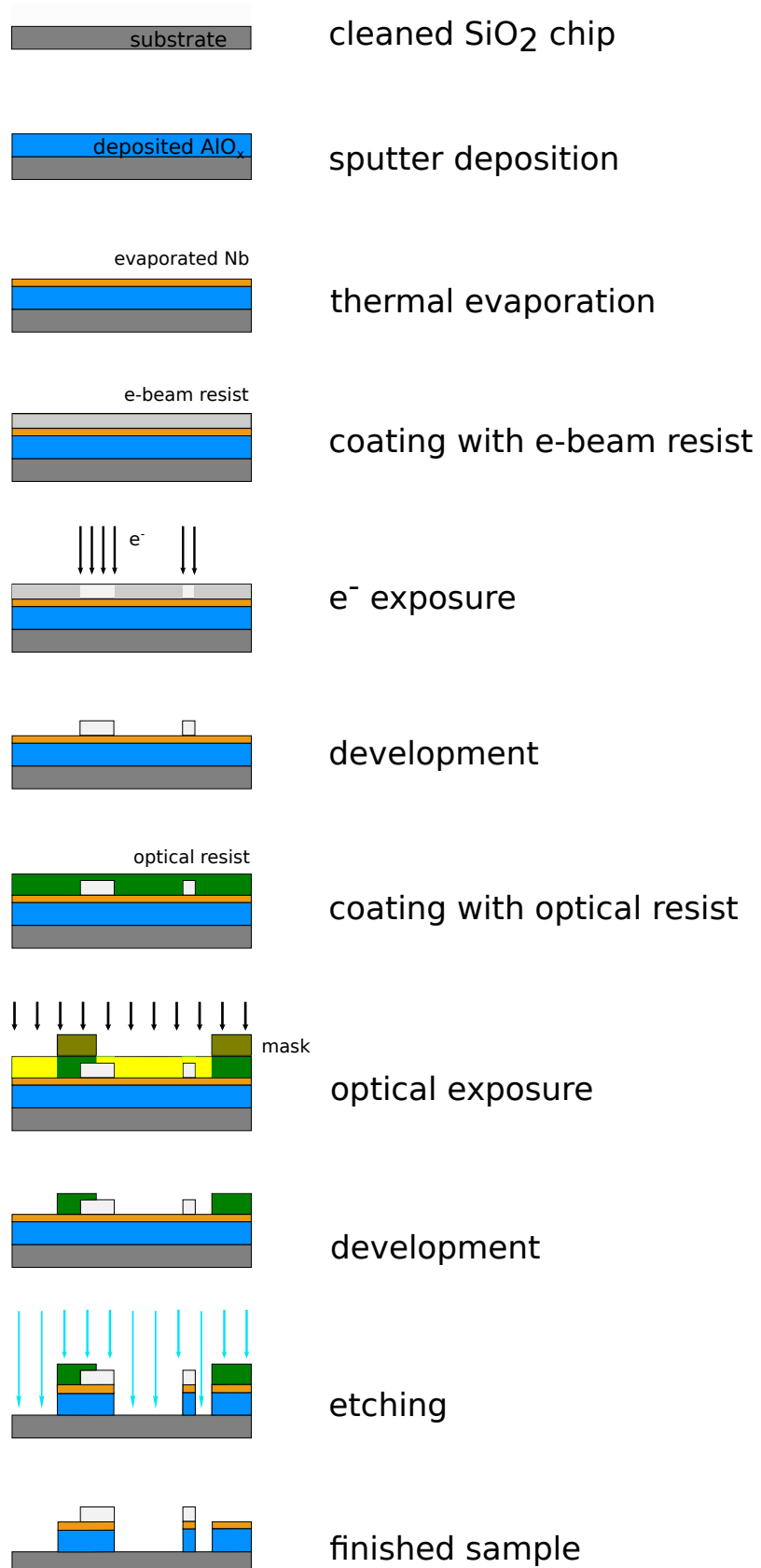


Figure A.1: Schematic overview of the fabrication process.

B Manual controlled film evaporation in the *PLASSYS MEB 550s*

First, plug the manual controller into the *Telemark Digital Sweep* module and set the "control select" on the *Telemark ST Controller* to "local".

Install the chip onto the sample holder and pump the load lock to a transfer pressure of about 10^{-6} mbar. Rotate the sample holder in the "evaporation" position and open the valve to the main chamber. Select the crucible and pump to $3 \cdot 10^{-7}$ mbar. After setting the high voltage to 10 kV and turning the electrode filament on, it is important to wait some time to allow the filament to warm up slowly. The current in the filament has to be ramped up slowly for the same reason. Inside the load lock, there is a crystal oscillator to determine the film growth rate and the film thickness. Ramp the filament current up until the crystal oscillator shows the aimed growth rate. Open the substrate shutter after the processes are stabilized and reset the film thickness monitor. During the evaporation, the filament current has to be checked constantly and may need some adjustment to get a constant growth rate.

Close the substrate shutter as soon as the monitors shows the appropriate film thickness and turn the filament current turned down. The current and the high voltage can be shut down after a short waiting time. Close the valve to the main chamber and rotate the sample holder back into the "load" position. The load lock can be vented.

Acknowledgements

I want to express my gratitude to Prof. Dr. Alexey V. Ustinov for giving me the opportunity of working on this extremely interesting topic in his research group and for the chances to participate the Ski Seminar, the 2014 PTB “Cryoelectronic Components” workshop in Berlin and the upcoming 2015 DPG spring meeting in Berlin.

I want to thank Prof. Dr. Alexander Shnirman for being the second reviewer of this thesis.

My sincere thanks go to Dr. Hannes Rotzinger for being my supervisor. With his knowledge to almost any topic he provided me with answers, information and always a funny anecdote. Besides that, he was a source of ideas on how to approach the next challenge during this thesis.

A very big “Thank you” goes to Sebastian Skacel for supporting me throughout this thesis in all areas. With his helpful nature, he provided me with assistance in any kind.

My thanks go to Dr. Silvia Diewald (CFN-NSL) for operating the e-beam writer to fabricate the chips.

I would like to thank Sebastian Probst for the occasional sip of whisky and the conversations while enjoying it, scientific and non-work-related.

Big thanks go to the whole Ustinov group for this wonderful year, especially my “roommates” for the atmosphere in our office in 4-10.

Last but (definitely!) not least, I want to thank my parents and my brother for their full support in all areas of my life.